Journal of Water Process Engineering 82 (2026) 109482

Contents lists available at ScienceDirect

Journal of Water Process Engineering

journal homepage: www.elsevier.com/locate/jwpe

"Nickel and cobalt catalysis in biomass carbonization for bio-anodes in microbial fuel cells: Impact on structure and electrochemical performance"

Ahmed Abotaleb [a], Ashraf Ahmed [b,*], Dina H. Amin [c], Toka Khairy [c], Khaled A. Abd El-Rahem [d], Abeer El Shahawy [a,*]

[a] Department of Civil Engineering, Faculty of Engineering, Suez Canal University, P.O. Box 41522, Ismailia, Egypt
[b] Department of Civil and Environmental Engineering, Brunel University London, Kingston Lane, Uxbridge, UB83PH, United Kingdom
[c] Department of Microbiology, Faculty of Science, Ain Shams University, Cairo, 1566, Egypt
[d] Chemistry Department, Faculty of Science, Al-Azhar University, Assiut Branch, P.O. Box 71524, Egypt

ARTICLE INFO

Editor: Amir Razmjou

Keywords:
Microbial fuel cells
Biomass carbonization
Cabbage waste
Nickel and cobalt catalysis
Bioanode performance
Electrogenic bacteria

ABSTRACT

The anode is a very critical element that affects the performance of microbial fuel cells(MFCs). Carbonization of biomass has proven to be a sustainable and efficient technique for making carbonaceous 3D anodes for MFCs. Moreover, transition metals are known for their catalytic potential in the carbonization process and electrochemical devices. In this study, we catalyze the carbonization of cabbage core waste using Nickel and Cobalt through a very simple technique and use them as anodes in double-chamber MFCs. The morphology and structure of the resulting electrodes were compared to those of the same type of biomass carbonized without modification.

Additionally, their electrochemical performance was compared by using them in MFCs. The maximum power density values obtained were 904.6, 170.3, 71.2, and 42 mW/m^2 for the CW-800, Ni-800, Co-800, and carbon felt, respectively. The decrease in power density in MFCs assembled with the modified anodes can be attributed to the toxicity of the metals to the microorganisms. The findings of this study highlight the importance of balancing the concentration of doped metals in anodes used in MFCs. This work supports the advancement of the UNSDGs by contributing to Goals 6 (wastewater reuse), 7 (renewable bioenergy), 9 (low-cost green technologies), and 12 (circular resource use). The integration of microbiological and materials analysis offers a robust pathway for developing eco-friendly, high-performance MFC anodes.

1. Introduction

Wastewater is a rich source of energy, as it contains around 4–10 times the amount of energy required to treat it conventionally, stored as chemical energy [1]. Microbial electrochemical systems are innovative and sustainable devices that can clean wastewater of both organic and non-organic pollutants and extract energy from the wastewater [2]. They can harvest this energy in the form of bioelectricity energy (in a setup called microbial fuel cells) or biogas (in a setup called microbial electrolysis cells) without producing any toxic substances [3]. Microbial electrochemical cells are based on using active electrogenic microorganisms as a catalyst to oxidize pollutants in wastewater in an anaerobic environment, producing protons, electrons, and carbon dioxide; electrons are captured using an electrode called the anode and are transferred to the cathode through the external circuit while protons migrate inside the cell to the cathode [4]. A microbial fuel cell (MFC) can be configured in either a single-chamber or double-chamber design. In a double-chamber microbial fuel cell, the anode solution (anolyte) and cathode solution (catholyte) are separated using a proton exchange membrane, while the single-chamber configuration doesn't need a catholyte since it uses oxygen in the air as an electron acceptor [5]. Although the double-chamber configuration is more frequently used, the single-chamber configuration is more favorable since it's more economical and easier to scale up than the double-chamber configuration [6].

There are so many factors that affect the performance of MFCs, such as the morphology and chemical composition of the anode and the cathode, the type of used anolyte substrate and its degree of

* Corresponding authors.
E-mail addresses: ahmedelsayed12@eng.suez.edu.eg (A. Abotaleb), ashraf.ahmed@brunel.ac.uk (A. Ahmed), dina.hatem@sci.asu.edu.eg (D.H. Amin), tokakhairy@sci.asu.edu.eg (T. Khairy), khaledali_npp@yahoo.com (K.A. Abd El-Rahem), abeer_shahawi@eng.suez.edu.eg (A. El Shahawy).

https://doi.org/10.1016/j.jwpe.2026.109482
Received 28 August 2025; Received in revised form 4 January 2026; Accepted 7 January 2026
Available online 16 January 2026

degradability, the characteristics and conductivity of the proton exchange membrane, the distance between the electrodes, the cell configuration and the internal and external resistance of the cell [7]. The low power generation and high cost are the main drawbacks that prevent the commercialization of microbial fuel cells, which require more in-depth studies to overcome the problems that hinder power generation in microbial fuel cells [8]. One of the most important factors affecting the performance of microbial fuel cells is the anode. A good anode must be highly conductive, microbe-compatible, chemically and physically stable, and economically cheap [9]. The most widely used material for microbial fuel cell electrodes is carbon, such as carbon felt, carbon cloth, carbon paper, graphite rods, and carbon brushes, due to its high microbial compatibility, high surface area, good conductivity, low cost, and relative stability under cell operation conditions [10]. However, the microstructure of commercially available carbon anodes offers a relatively small surface area for microorganism colonization and biofilm formation, resulting in low power density output from MFCs [11]. To mitigate this problem, researchers have studied modifying the surface of carbon electrodes with nanomaterials such as carbon nanotubes (CNTs), graphene oxide (GO), and transition metal nanoparticles [12–15]. Moreover, another method to improve power generation in microbial fuel cells is the use of 3D carbon electrodes. 3D electrodes provide a significantly larger surface area for bacterial biofilm formation and enhanced ion diffusion through electrode pores [16]. One of the most common techniques for making 3D carbon electrodes is the carbonization of biomass and agricultural residues [17]. Carbonization of biomass and natural carbon precursors is an environmentally friendly method for making sustainable and eco-friendly 3D carbon electrodes. The direct carbonization of natural polymers and agricultural residues yields highly porous carbon materials with excellent electrical properties, resulting from the evaporation of moisture during the process. Additionally, heteroatoms such as nitrogen, phosphorus, sulfur, and silicon present in plants serve as self-dopants during the carbonization process. Those dopants can increase biocompatibility and enhance the extracellular electron transfer process during cell operation [18]. Cabbage and other brassicas are among the most abundant vegetables grown in the world with worldwide production estimated at 71.4 MMT in 2017 corresponding to 6.5% of vegetables production [19]. The waste produced from cabbage is relatively cellulose-rich with its stalk consisting of 37% cellulose on a dry-weight basis and has a relatively high trace minerals concentration which are essential for heterogeneous doping [20]. The carbonization of cellulose-rich carbon precursors yields biochar with lower hydrogen to carbon ratio (H/C) which indicates higher stability [21]. Moreover, cellulose is easier to carbonize than lignin which leads to formation of carbonaceous materials with high porosity and high surface area which are favorable in microbial electrochemical systems. Carbon anodes that are made from precursors with high cellulose content demonstrate better extracellular electron transfer but lower specific capacitance [22].

While numerous studies have explored biomass-derived carbon materials for anodes in MFCs [23–30], many focus solely on electrochemical characterization and neglect microbial responses to surface modifications. This study is novel in two key aspects. First, it employs cabbage core waste, an abundant yet underutilized agricultural residue, which is catalytically carbonized with nickel and cobalt nanoparticles to form a carbonized cabbage structure, compared with plain carbonized cabbage core. This approach enables the fabrication of bio-anodes using a simple and scalable method. Cabbage stalk is a very robust agricultural waste with no commercial applications, which makes it an excellent carbon precursor for MFC bio-anodes. The changes in structure, morphology, and chemical composition resulting from the addition of metal ions to the proposed electrodes were investigated. Second, and most distinctively, this study integrates the effect of adding metal nanoparticles on microorganisms, as demonstrated, with microbial community analysis to examine the biocompatibility and microbial colonization of each modified electrode. This study combines electrochemical testing with 16S rRNA gene sequencing and biochemical identification to track how *Citrobacter freundii* and *Klebsiella variicola*, two electrogenic strains, respond to nickel- and cobalt-doped surfaces. While previous research has reported enhanced conductivity via metal doping [31–36], few have investigated its trade-offs with microbial toxicity or shifts in strain-specific colonization dynamics under real wastewater conditions. Our microbial analysis thus provides crucial insights into the observed decline in MFC performance despite improved material properties, bridging the gap between materials science and microbial ecology in MFC design and highlighting the importance of studying electrogenic extremophilic microorganisms for MFC application.

Table 1
The measured water quality parameters and the measurement techniques.

Wastewater quality parameter	Standard Method	Value	Unit
pH	pH meter (Adwa AD 1030 pH Benchtop Meter)	5.5	
BOD	5 Days of incubation at 20 °C	22,500	mg/
Total Suspended Solids	Suspended Solids dried at 103–105 °C	56,840	l
COD	Closed Reflux method (V-730 Double Beam UV–Visible Spectrophotometer)	72,000	
Total Dissolved Solids	Dissolved Solids dried at 103–105 °C	33,440	

2. Materials and methods

2.1. Materials

Plain carbon felt (CF) was purchased from Fuel Cell Store USA. Phosphate buffer solution was purchased from Power Chemical. Egypt. Potassium ferricyanide was bought from ADVENT Chembio. Nickel(II) acetate tetrahydrate and Cobalt(II) acetate tetrahydrate were purchased from Sigma-Aldrich, USA. Cabbage core waste was obtained from a local market in Egypt and used without further treatment.

2.2. Wastewater characteristics

Wastewater that was used as anolyte was collected from a local sugarcane juice shop during the machine-washing stage. Water characteristics were measured according to standard methods for the examination of water and wastewater, as determined by the American Public Health Association (APHA) [37], and are presented in Table 1.

2.3. Anode preparation

Cabbage core waste was collected from a local market, washed with water to remove impurities, dried at 80 °C, and weighed. Nickel and Cobalt solutions were prepared as follows. 1% wt of nickel acetate and cobalt acetate were added separately into flasks containing 200 ml of deionized water and were stirred until complete dissolution. Then, equal parts of cabbage core were added to the flasks and left to soak for 24 h. For comparison, a similar piece of cabbage core was carbonized without any modifications. For the carbonization process, the tube furnace was sealed tightly and vacuumed to create an oxygen-free environment. The carbonization process was carried out at a heating rate of 2 °C/min and held for 2 h at a temperature of 800 °C. The prepared carbon anode was wrapped with a copper wire to serve as a current collector.

2.4. MFC construction and operation

The study was conducted in batch mode using a double-chamber microbial fuel cell setup. The body of the cell was constructed by connecting the anode and cathode chambers (500 ml chambers with

Table 2
The primers used in this study.

Gene	Primer	Primer sequence 5'-3'	Amplified product	Reference
16S rRNA	*F27* R1492	AGAGTTTGATCMTGGCTCAG TACGGYTACCTTGTTACGACTT	1485 bp	[39]

dimensions of 5 cm × 10 cm × 10 cm) with a proton exchange membrane between them. Sulfonated polystyrene with a thickness of 250 μm was prepared as described in [38] and utilized as a proton exchange membrane. The as-prepared anode was immersed in the anolyte within the anode's chamber. A small hose was added to the anode chamber, and its end was immersed in a water basin to prevent gases from accumulating in the anode chamber. For comparison, a piece of carbon felt with dimensions of 4 cm × 4 cm was used as a commercially available anode. A piece of carbon felt with dimensions of 4 cm × 4 cm was used as a cathode in all assembled microbial fuel cells. The cathode chamber was filled with potassium ferricyanide (K_3]Fe(Cn)$_6$[) (50 mM) in PBS solution (50 mM). The cells were operated at room temperature (27 °C) for 7 days, during which the anode chamber was kept tightly closed to maintain an anaerobic condition. The open-circuit voltage was recorded using an Arduino-based data logger at one-hour intervals. After the open-circuit voltage stabilized, the cell circuit was closed by connecting the current collectors of the anode and the cathode with a Potentiostat/Galvanostat (AMEL Model 2550). The connection was established by connecting the working electrode to the anode's current collector and both the counter electrode and the reference electrode to the cathode current collector. Linear sweep voltammetry (LSV) was performed, with the maximum stable open-circuit voltage (OCV) measurement set as the initial potential value and zero as the final potential value. LSV was performed at a scan rate of 1 mV/s, and the (I-V) curve was recorded for all assembled cells. Cyclic voltammetry was carried out with a voltage window of 600 mV to −250 mV at a scan rate of 1 mV/s.

2.5. Characterization

The mineralogical composition and crystallographic structure of the carbonized samples were analyzed through the X-ray diffraction technique (XRD), and it was obtained from Bruker Co. model D8 (including reflectometry, high-resolution diffraction, in-plane grazing incidence diffraction (IP-GID), small-angle X-ray scattering (SAXS), as well as residual stress and texture investigations).

The morphology of the prepared anodes' surface was investigated using a scanning electron microscope (SEM) equipped with an energy dispersive spectrometer (JSM-IT210).

Surface area, pore size, and pore volume were measured by the Brunauer-Emmett-Teller (BET) analyzer model Nova Touch LX2, manufactured by Quanta Chrome Company in the USA. The measurements are done using the standard volumetric method by nitrogen adsorption at K.

The functional groups of the prepared electrodes were determined using Fourier-transformed infrared spectroscopy (FTIR) with a PerkinElmer 1720-X spectrometer. The spectra were scanned between 4000 and 400 cm^{-1} with a resolution of 2.00 cm^{-1} on samples pelletized using a press in potassium bromide, with a proportion of 1 mg of product per 100 mg of KBr.

2.6. Bacterial analysis

2.6.1. Isolation of bacteria from the anode

Microorganisms were isolated from the surface of the bio-anode using a sterile swab technique followed by serial dilution and cultivation on nutrient agar. The bio-anode surface was gently swabbed using a sterile cotton swab to collect the attached biofilm. The swab was then immersed in a sterile test tube containing 10 ml of sterile distilled water and vortexed for 30 s to release the microbial cells into suspension. To reduce microbial density and facilitate the Isolation of distinct colonies, serial dilutions were performed by transferring 1 ml of the swab suspension into 9 ml of sterile distilled water, sequentially diluting the sample up to 10^{-5}. From each dilution, 100 μl was plated onto nutrient agar using a sterile spreader to ensure even distribution. The plates were incubated at 30 °C for 24 to 48 h. After incubation, colonies were examined for morphological diversity, and representative colonies were selected for purification. Purification was achieved by repeatedly streaking individual colonies onto fresh nutrient agar plates until a uniform colony morphology was observed, indicating the presence of pure cultures. For long-term preservation, purified isolates were suspended in sterile nutrient broth containing 20% glycerol and stored at −20 °C.

2.6.2. Biochemical identification using VITEK

Microorganism identification for the selected strains (S2–S3) was carried out using the VITEK® MS system (bioMérieux, France), which operates on Matrix-Assisted Laser Desorption Ionization Time-of-Flight Mass Spectrometry (MALDI-TOF MS) technology (bioMérieux, 2025). The isolates were sub-cultured under anaerobic conditions at 37 °C. They were initially grown in nutrient broth for general culturing. The nutrient broth was prepared using Sigma-Aldrich Nutrient Broth (pH 7.0), and the cultures were incubated for 24 h with shaking at 200 rpm to promote optimal growth. After incubation in nutrient broth, the cultures were plated onto nutrient agar plates (also from Sigma-Aldrich) to isolate individual colonies. The nutrient agar was prepared according to the manufacturer's instructions and poured into petri dishes to a depth of 1.5 cm. The plates were incubated at 37 °C for 24–48 h to allow colony growth. Isolated colonies were subcultured into fresh nutrient broth to ensure purity and were then prepared for VITEK MS analysis.

Fresh colonies were transferred onto a VITEK MS-DS target slide, overlaid with 1 μL of α-cyano-4-hydroxycinnamic acid (CHCA) matrix solution, and allowed to air-dry. The prepared target slide was inserted into the VITEK® MS device, and mass spectra were acquired according to the manufacturer's default protocol. Identification was achieved by matching the acquired spectra to the VITEK MS database, following the guidelines outlined in the CSEFRA-WI-29 equipment manual.

2.6.3. Molecular identification of the selected bacterial strains

2.6.3.1. DNA extraction. Genomic DNA was extracted from bacterial samples (S2-S3) using the QIAamp DNA Mini Kit (QIAGEN, Germany), following the manufacturer's protocol (Table 2). Briefly, 20 μL of QIAGEN protease was added to the bottom of a 1.5 ml microcentrifuge tube, followed by 200 μL of the sample. Then, 200 μL of Buffer AL was added and mixed by pulse vortexing for 15 s. The mixture was incubated at 56 °C for 10 min. After a brief centrifugation to remove droplets from the lid, 200 μL of 96% ethanol was added, and the mixture was remixed by vortexing. The lysate was transferred to a QIAamp Mini spin column, placed in a 2 ml collection tube, and centrifuged at 8000 rpm for 1 min. The column was then washed sequentially with 500 μL of Buffer AW1 and Buffer AW2, each followed by centrifugation. A final centrifugation step was performed to remove the residual wash buffer. DNA was eluted by adding 100 μL of Buffer AE to the column, incubating at room temperature for 1 min, and centrifuging at 8000 rpm for 1 min. The eluted DNA was stored at −20 °C until further use.

2.6.3.2. Preparation of PCR master mix. Polymerase Chain Reaction (PCR) amplifications were performed using the Emerald Amp GT PCR Master Mix (2× premix) (Takara, Code No. RR310A) following the manufacturer's protocol. For each 25 µl reaction, the PCR mixture was prepared by combining 12.5 µl of the 2× premix with 4.5 µl of PCR-grade water. To this, 1 µl each of forward and reverse primers (20 pmol) was added, followed by 6 µl of template DNA. The final reaction volume was adjusted to 25 µl. The thermal cycling conditions for the amplification of the target 16S rRNA gene were optimized based on Emerald Amp GT PCR Master Mix manufacturer. The cycling protocol began with an initial denaturation step at 94 °C for 5 min. This was followed by 35 cycles of denaturation at 94 °C for 30 s, annealing at 56 °C for 1 min, and extension at 72 °C for 1 min. A final extension step was performed at 72 °C for 10 min to ensure complete amplification of the target DNA fragments. A DNA molecular weight marker was prepared by gently mixing the ladder through pipetting to ensure homogeneity. A volume of 6 µl of the marker was directly loaded onto the agarose gel alongside the PCR product samples for molecular weight estimation.

2.6.3.3. Agarose gel electrophoresis. Agarose gel electrophoresis was carried out following the method described by [40] with minor modifications. Briefly, 1 g of electrophoresis-grade agarose was dissolved in 100 ml of TBE buffer by heating in a microwave oven with intermittent swirling until it was fully dissolved. The molten agarose was cooled to approximately 70 °C, after which ethidium bromide was added at a final concentration of 0.5 µg/ml and mixed thoroughly. The warm agarose was then poured into a gel casting tray fitted with an appropriate comb and allowed to solidify at room temperature.

Once the gel had been set, the comb was carefully removed, and the electrophoresis tank was filled with TBE buffer. Twenty microliters of each PCR product, along with the positive and negative controls, were loaded into individual wells of the gel. Electrophoresis was conducted at a constant voltage of 1–5 V per centimeter of the tank length for approximately 30 min. After the run was completed, the gel was transferred to a UV transilluminator for visualization. Gel images were captured using a gel documentation system, and the resulting data were analyzed using computer software.

2.6.3.4. 16S rRNA sequencing and phylogenetic analysis of the selected bacterial strains. The phylogenetic tree of S2 and S3 strains was constructed based on 16S rRNA gene sequences to determine their evolutionary relationships. The sequences were obtained from publicly available databases and aligned using the MUSCLE algorithm (Edgar, 2004) in Geneious Prime software (https://www.geneious.com/series/multiple-alignments). The aligned sequences were then used to generate a phylogenetic tree using the FastTree option in Geneious software. FastTree computes approximately maximum-likelihood phylogenies with efficient heuristics [41], providing reliable branch support values. The tree topology was assessed, and branch support values (posterior probabilities) were indicated at the nodes, with values closer to 1 signifying stronger statistical confidence in the branching patterns. To enhance the visual interpretation of the phylogeny, different clades were colour-coded to distinguish major taxonomic groupings. The scale bar represents genetic distance (0.005), illustrating the degree of sequence divergence among the strains. The final tree was exported and annotated for presentation.

3. Results and discussion

The primary objective of this study is to investigate the differences in catalytic potential between cobalt and Nickel in MFCs and their impact on electrochemical performance. It's well known that transition metals are used to catalyze the carbonization process, enhancing the structure of the resulting material and imparting superior properties to it. Here, we use Nickel and Cobalt nanoparticles as catalysts for the carbonization of cabbage stalk and employ the resulting material as an anode in a microbial fuel cell fed with extremely polluted industrial wastewater. The metal concentration was kept low to prevent metal particles from closing the pores of the carbonized material. To evaluate the effect of incorporating Nickel and Cobalt nanoparticles, a piece of cabbage stalk was carbonized without any modifications. Carbonized samples were labeled as Ni-800, Co-800, and CW-800.

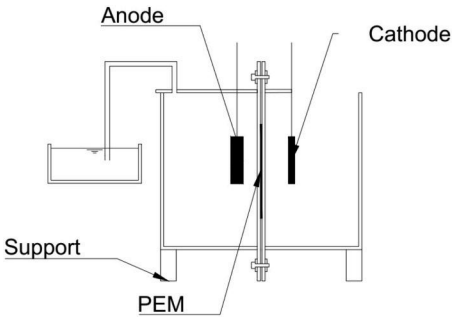

Fig. 1. Schematic diagram for the MFC design used.

3.1. Characterization of obtained anodes

3.1.1. Scanning electron microscope

The formation of biofilm layers on the surface of the carbonized samples confirms the successful bacterial colonization of the material's surface. Additionally, the use of agricultural waste (cabbage stalk) as a precursor for the anode aligns with the principles of sustainability and circular economy, making it an environmentally friendly alternative to conventional anode materials. SEM images of all carbonized samples, both before and after use in the cells, are shown in Figs. 1(A-F).

SEM images provide critical insights into the morphology of the proposed samples' surfaces and the interaction between the anode and electroactive microorganisms in the anolyte. By comparing the morphological structure of the three proposed samples, it can be observed that the CW-800 and Ni-800 samples possessed a plain surface with many honeycomb-like pores distributed over the whole surface of the samples. The diameter of the pores in the CW-800 sample is slightly bigger than the pore diameter of the Ni-800. A higher pore diameter allows for easier diffusion of ions and microorganisms into the inner layers of the electrode, providing an adequate environment for microorganism colonization and biofilm formation [42]. This maximizes the contact between electroactive microorganisms and significantly enhances the performance of the microbial fuel cell. As for the Co-800 sample, SEM images reveal a more complex surface morphology with sharp edges and a range of pore diameters. In general, smaller pore diameters are unfavorable for the long-term operation of MFCs, as they tend to become blocked entirely at the beginning of cell operation due to biofilm formation, which prevents ion diffusion into the inner layers of the anode [43].

On the other hand, SEM images of the electrodes after 7 days of operation inside the cells provide crucial insights into the degree of biocompatibility and the amount of biofilm that formed on the electrode surface. The CW-800 sample demonstrated the highest biocompatibility with a very thick layer of biofilm on its surface, followed by the Ni-800 sample. As for the Co-800 sample, it showed very poor biocompatibility with a much less thick biofilm observed on its surface.

Biocompatibility is a crucial factor in the operation of microbial fuel cells, significantly affecting the electrochemical performance of the cell. Higher biocompatibility leads to faster colonization for electroactive microorganisms, which substantially increases the amount of electrons generated on the electrode's surface [42].

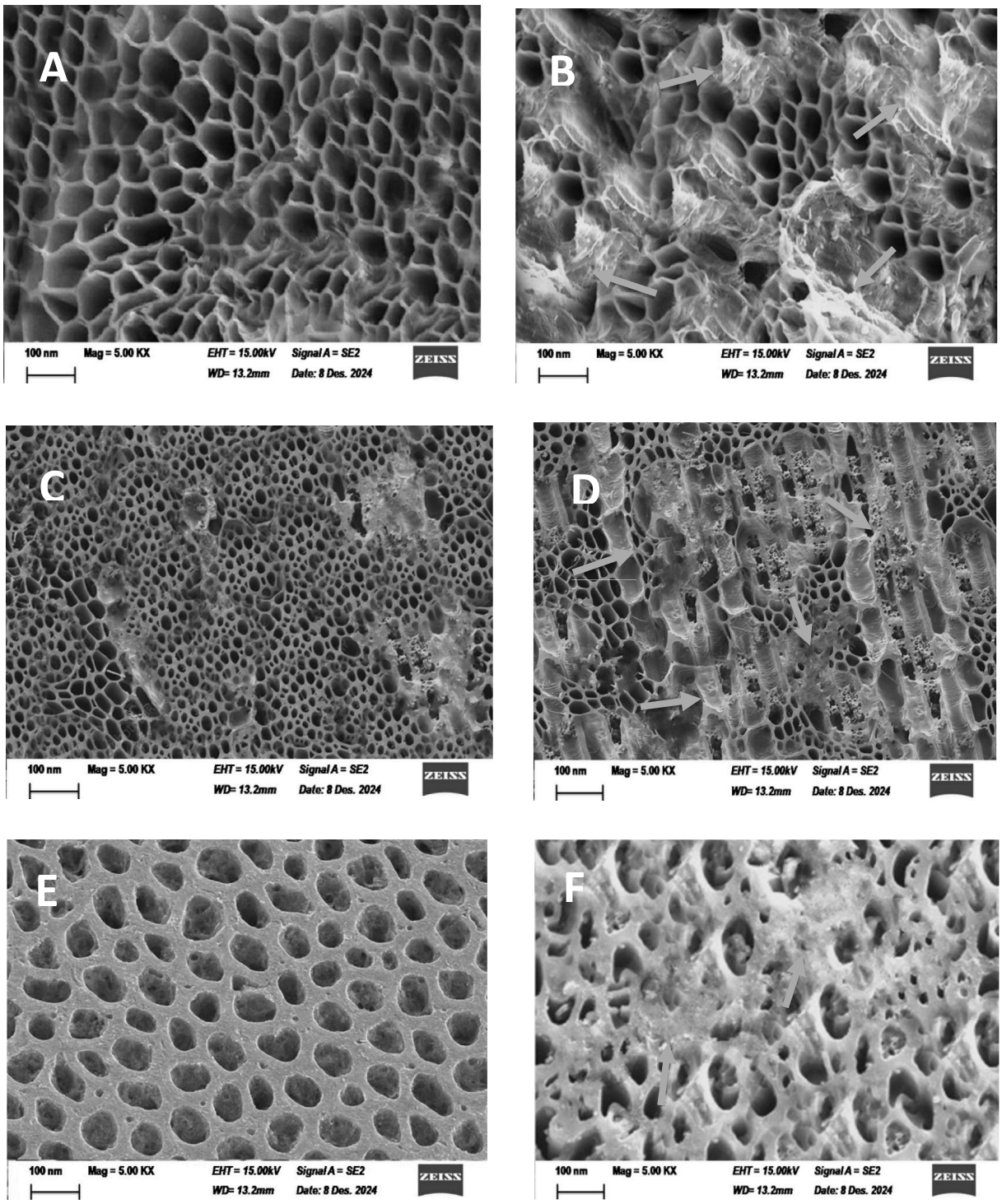

Fig. 2. SEM images of the CW-800 sample before using in the cell (A) and after using in the cell (B), Ni-800 sample before using in the cell (C) and after using in the cell (D), and the Co-800 sample before using in the cell (E) and after using in the cell (F).

3.1.2. XRD pattern

X-ray diffraction (XRD) analysis was carried out to investigate the structural properties of the carbonized samples. The XRD pattern of the CW-800 demonstrated two broad peaks with 2θ values of approximately 22.5° (high intensity) and 42° (lower intensity). The first peak is indicative of the (002) plane of graphitic carbon, which corresponds to the stacking of graphene layers in a disordered or turbostratic structure. The broad nature of the peak suggests the presence of amorphous carbon or partially graphitized carbon, which is typical for biomass-derived carbon materials. It can be concluded from the high intensity of this peak that a significant degree of carbonization is achieved, where organic materials present in the cabbage stalk (such as cellulose, hemicellulose, and lignin) have been converted into carbon. The broad nature of this peak indicates a low degree of crystallinity and that the material implies defects or disordered carbon atoms. This can be attributed to the low carbonization temperature of 800 °C, which is sufficient to decompose most organic materials but not enough to form highly ordered carbon structures. The second peak at $2\theta \approx 42^{\circ}$

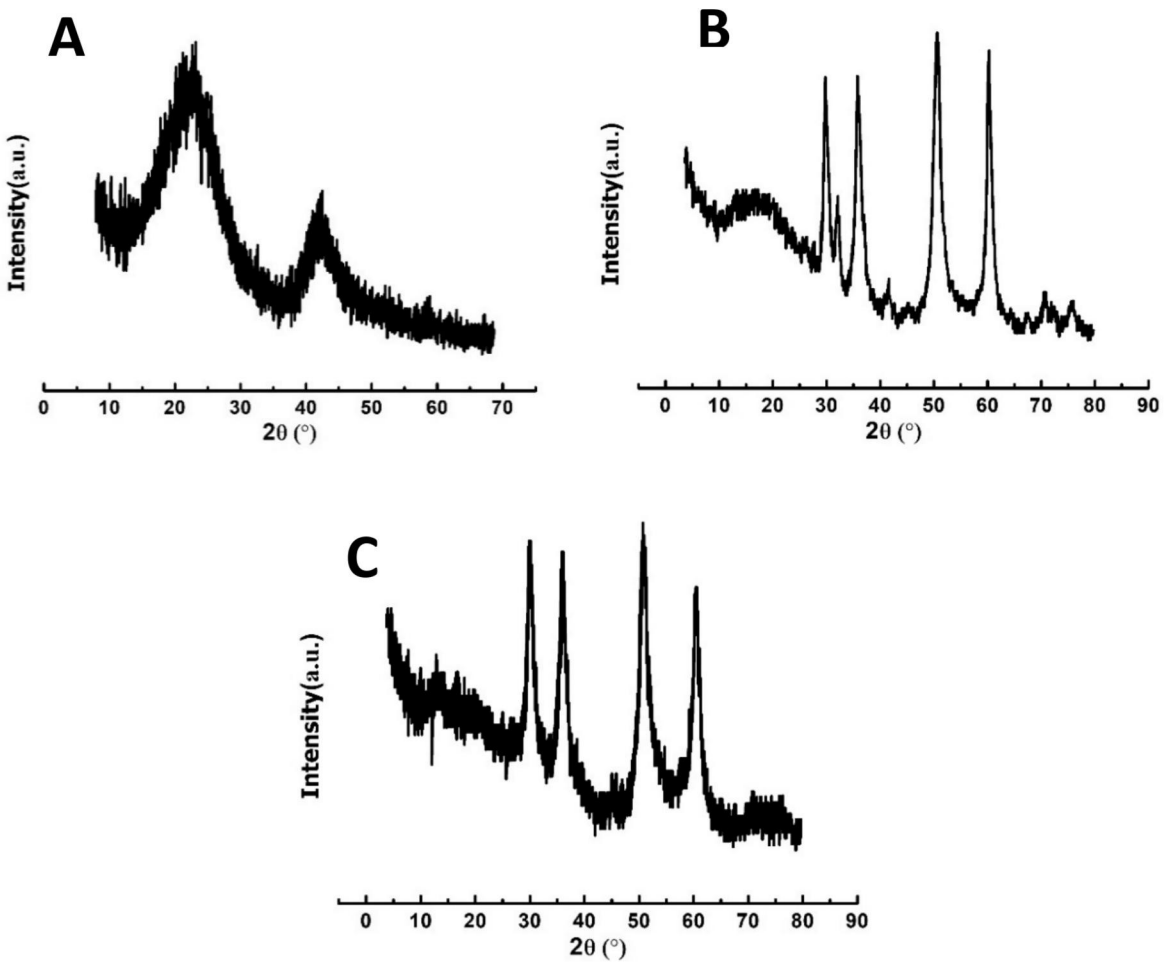

Fig. 3. XRD pattern of the (A) CW-800 sample, (B) Ni-800 sample, and (C) Co-800 sample.

corresponds to the (100) plane of graphitic carbon, which is associated with the in-plane structure of graphene layers. The fact that this peak has lower intensity than the (002) peak indicates that the sample is not completely carbonized. However, the presence of this peak confirms the formation of graphitic domains within the carbonaceous material's structure [44]. The disordered structure of carbon atoms and the low crystallinity of the graphite domains in the sample are attributed to the low degree of carbonization, resulting in partial graphitization. However, the mixed structure of the material is favorable for microbial fuel cell operation, as the amorphous structure provides a higher surface area for bacterial colonization, while the crystalline structure increases electrical conductivity and enhances the extracellular electron transfer process [28].

The diffractogram of the Ni-800 sample demonstrates several sharp peaks indicating the presence of several crystalline materials within the sample. The sharp peaks at $2\theta = 37.2°$, 42.1°, and 62.9° correspond to Nickel Oxide (PDF#00–047-1049). The peaks at $2\theta = 44.5°$, 51.8°, and 76.9° correspond to the presence of Nickel particles (PDF#00–004-0850). The sample also contained crystalline Nickel Hydroxide, as evidenced by the presence of peaks at $2\theta = 32.1°$ and 71.9° (PDF#00–014-0117). The presence of these crystalline materials inside the carbon anode has a great potential to increase the conductivity of the electrode and enhance the extracellular electron transfer process.

As for the Co-800 sample, the XRD pattern shows four main sharp peaks at $2\theta = 29.4°$, 36.5°, 51.5°, and 61.5°, which are expected to correspond to Calcite (PDF#00-024-0072), Cobalt oxide (PDF#00-043-1004), and Metallic Cobalt (PDF#00-005-0727) (Fig. 2(A-C).

These results confirm the complete decomposition of cobalt acetate and nickel acetate during the carbonization process, as well as the reaction of the resulting metallic atoms with the samples.

3.1.3. FTIR spectroscopy

The Fourier-transform infrared (FTIR) spectrum of the graphitized samples provides critical information about functional groups and chemical bonds present in the samples, which can play a significant role in enhancing the electrochemical performance of the microbial fuel cell. The CW-800 spectrum shows broad peaks at 3450 cm^{-1} and 3310 cm^{-1} attributed to the O—H vibrations, which may correspond to hydroxyl groups (OH). The broadness of this peak can refer to the presence of adsorbed water, hydrogen-bonded hydroxyl molecules, which are very common in biomass-based materials. The presence of hydroxyl groups is beneficial for microbial fuel cells' operation, as they increase the hydrophilicity of the anode and enhance microbial adhesion to its surface [45,46]. These groups can participate in redox reactions, facilitating electron transfer between the microbes and the anode [47]. The broad peak at 1630 cm^{-1} corresponds to C═C stretching vibrations in aromatic rings or conjugated systems, which is related to the graphitic domains present in the sample.

Additionally, the peak at ~1730 cm^{-1} corresponded to C═O stretching vibrations of esters and carboxylic acids [48]. The significant decrease in transmittance from 905 cm^{-1} to 660 cm^{-1} is related to the C—H out-of-plane bending vibrations in aromatic hydrocarbons [49]. The very low transmittance at 660 cm^{-1} can be attributed to the high concentration of aromatic compounds in the sample, which is a common characteristic among carbon materials derived from natural biomass [50]. The sharp peak at 470 cm^{-1} can be associated with either C—C

Table 3
Pore volume and average pore diameter for the obtained anodes.

	Pore volume (cm^3/g)	Average pore diameter (nm)	Pore type
CW-800	0.21	3.5	Meso porous
Co-800	0.37	4.2	Mesoporous
Ni-800	0.41	2.8	Micro porous

bending vibrations or metal-oxygen (M–O) vibrations, depending on whether any metal impurities are present in the sample [51].

As for the Ni-800 FTIR spectrum, it displayed similar peaks to the Co-800 sample with distinct peaks at 3922 cm^{-1}, 3615 cm^{-1} and 3203 cm^{-1}, which can be corresponding to N—H, O—H, or C—H vibrations, along with a sharp peak at ~470 cm^{-1}, attributed to Ni—O stretching vibrations, confirming the presence of nickel precursors. Moreover, the broadening of the peak at ~1580 cm^{-1} suggests enhanced graphitization, potentially due to the catalytic effect of nickel. Additionally, the presence of a small peak at ~480 cm^{-1} indicated the retention of Ni-based species in the carbonized material [51].

The FTIR spectrum of the Co-800 sample resembled that of the Ni-800 sample but included a distinct peak at ~530 cm^{-1}, corresponding to Co—O stretching vibrations, confirming the successful doping with cobalt. A similar trend was observed, with the disappearance of hydroxyl and carbonyl peaks and the emergence of a strong band at ~1490 cm^{-1}, indicating the formation of graphitic carbon. The Co-doped sample also exhibited a sharp peak at ~540 cm^{-1}, corresponding to residual cobalt-based species, suggesting that cobalt remained dispersed in the structure after carbonization [52].

The FTIR spectra reveal that the carbonization process effectively decomposed the organic functional groups of the cabbage core, leaving behind a graphitized carbon structure. Both Ni and Co doping enhanced the graphitization, as evidenced by the more pronounced C═C stretching peak at ~1500 cm^{-1}, compared to the CW-800 sample. The retention of metal-based peaks in the Ni- and Co-doped samples suggests that the metals were successfully integrated into the structure, potentially enhancing the electrochemical properties of the anode materials (Figs. 3(A-C).

3.1.4. BET

The adsorption-desorption curves presented for the blank, Co-doped, and Ni-doped samples provide insights into the porous characteristics of these materials. These isotherms, analyzed in conjunction with the BET (Brunauer-Emmett-Teller) theory, reveal significant changes in surface properties resulting from carbonization and metal doping.

The adsorption-desorption curve for the CW-800 sample exhibits a Type IV isotherm with an H3 hysteresis loop (typical for mesoporous materials). This suggests the presence of slit-like pores formed during the carbonization process. The curve's adsorption branch indicates moderate uptake at low relative pressures ($P/P0 < 0.1$), associated with micropore filling, followed by a sharp increase at higher relative pressures due to multilayer adsorption and capillary condensation in

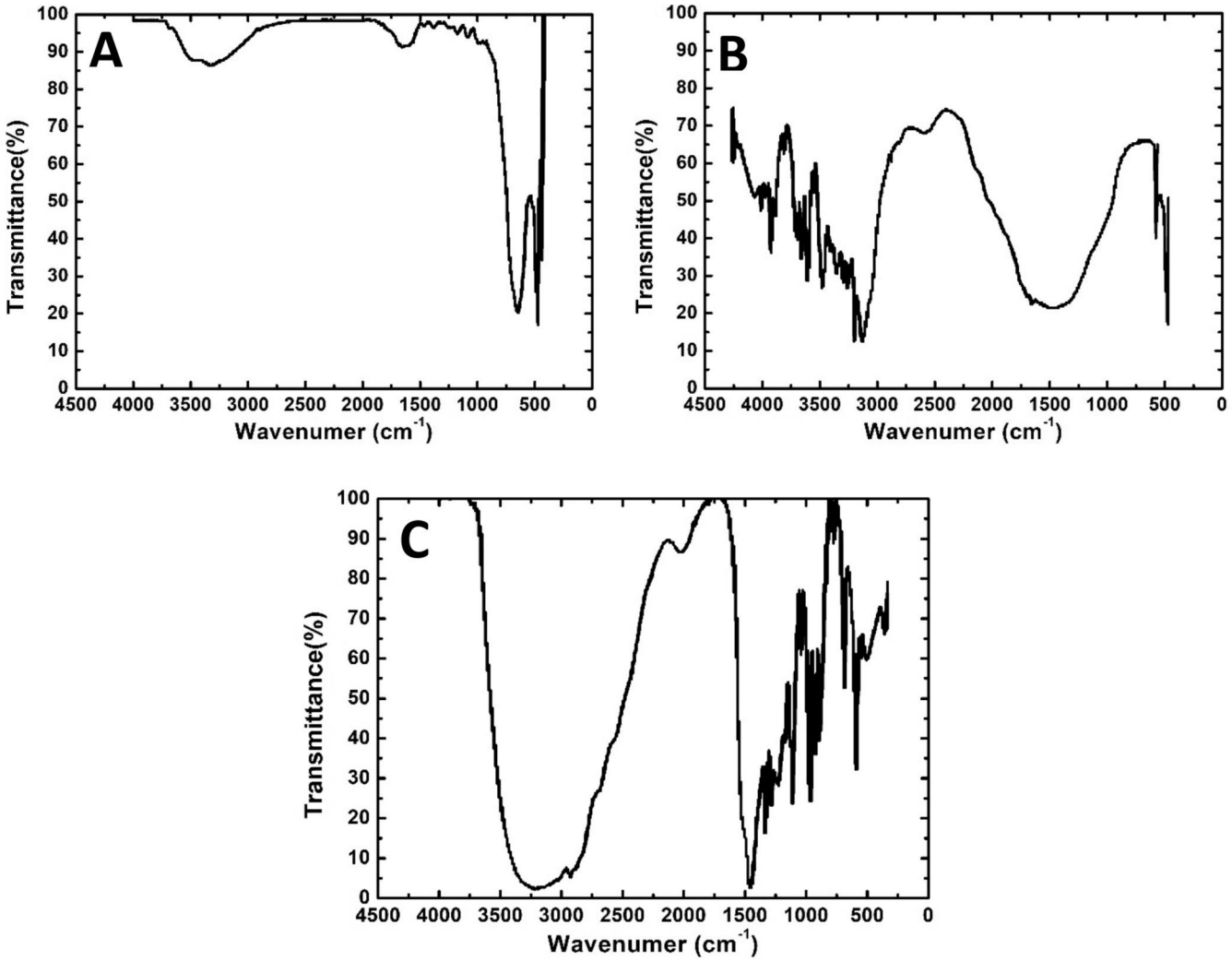

Fig. 4. FTIR spectra of the (A) CW-800 sample, (B) Ni-800 sample, and (C) Co-800 sample.

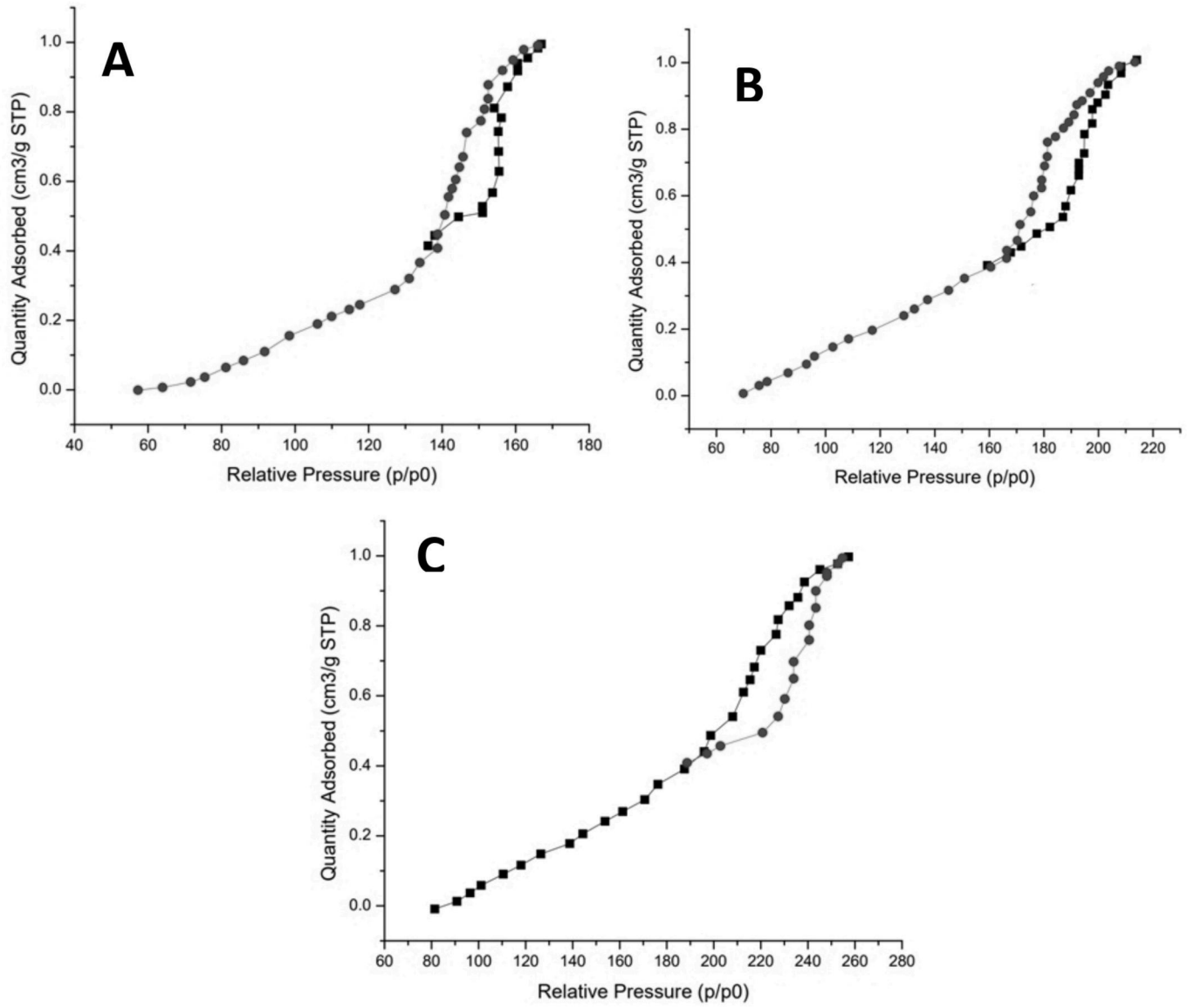

Fig. 5. Adsorption-desorption curve of the (A) CW-800 sample, (B) Co-800 sample, and (C) Ni-800 sample.

mesopores [53].

Cobalt doping facilitates the formation of a highly porous structure through catalytic graphitization during carbonization. This enhances the specific surface area and pore volume, which are critical for microbial biofilm formation and efficient extracellular electron transfer in microbial fuel cells. The Co clusters observed in SEM further support the notion that active sites are introduced, contributing to a higher adsorption capacity.

The adsorption-desorption curve for the Ni-doped sample is expected to exhibit higher adsorption at low relative pressures compared to the blank and Co-doped samples, indicating a significant presence of micropores. The hysteresis loop resembles H2, indicative of more complex pore networks and irregular shapes formed due to nickel's catalytic effect during carbonization.

Nickel doping not only enhances the microporous structure but also increases surface roughness, as observed in SEM images. The complex pore network improves the material's ability to adsorb and transport molecules, making it highly favorable for microbial activity and electron transfer. This structural enhancement aligns with reports of nickel's role in improving the electrochemical properties of carbon materials.

The pore volume and average pore diameter values obtained from BET align with the SEM images. Table 3 shows the pore volume and Average pore diameter values obtained from the BET analysis.

As for the BET surface area, the Ni-800 sample had the highest surface area of 342.7 m^2/g, followed by the Co-800 with a BET surface area of 289.3 m^2/g. The CW-800 had the lowest BET surface area with a value of 178.5 m^2/g. These results confirm the catalytic effect of metal nanoparticles on the carbonization process, which enhances the structure of the resulting carbonaceous materials (Figs. 4(A-c).

3.2. Performance of the assembled MFCs and electrochemical analysis

Modifying carbon materials by doping them with transition metal nanoparticles is a common technique because it can enhance the electrochemical performance of carbon materials by increasing conductivity and catalyzing oxidation and reduction reactions. Moreover, transition metal salts can catalyze the carbonization of carbon precursors, which enhances the morphology and chemical structure of the produced carbon material [54]. The experiment aims to study the effect of Nickel and Cobalt nanoparticles on the carbonization process of cabbage cores, to use them as bio-anodes in microbial fuel cells. It also investigates the electrochemical performance of the modified anodes during microbial

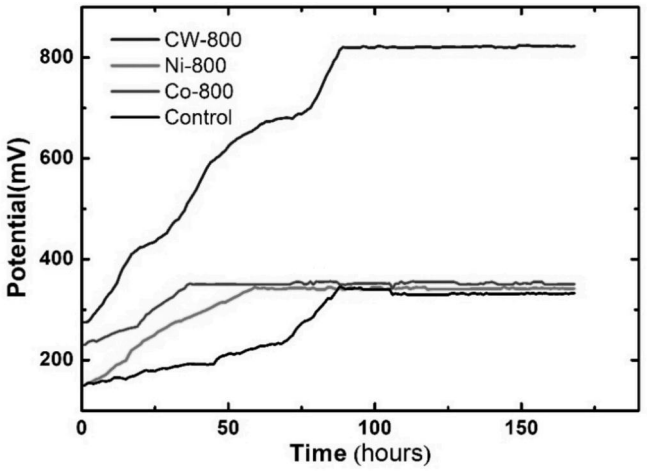

Fig. 6. Output OCV of assembled cells.

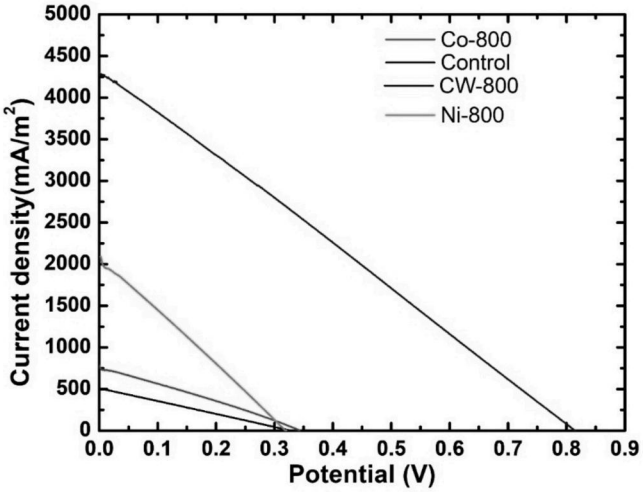

Fig. 7. Polarization curves for assembled cells.

fuel cell operation and compares it with that of non-doped carbonized cabbage cores. The cabbage core was carbonized without modification, and the cabbage core modified with Nickel and Cobalt was named CW-800, Ni-800, and Co-800, respectively.

To scientifically evaluate the performance of synthesized anodes, their electrochemical performance was compared with that of carbon felt, one of the most commonly used 3D carbon materials. One of the most important parameters for evaluating the performance of a microbial fuel cell is the open-circuit voltage (OCV). OCV can be defined as the difference in potential between the anode and the cathode of a fuel cell when there is no current flowing through the external circuit, and it represents the highest voltage value the cell can deliver as electrons accumulate on the anode, increasing its charge. In a microbial fuel cell, the open-circuit voltage (OCV) starts with a certain value and continues to increase until it reaches a maximum value; the period it takes to get the maximum OCV value varies based on several factors, including the time needed for biofilm formation and the kinetics of oxidation and reduction reactions within the cell [2]. To record the changes in OCV over the cell operation period, the cells were connected to data loggers, and OCV readings were recorded every 5 min. Fig. 5 shows the OCV values recorded from cells assembled with CW-800, Ni-800, and Co-800 anodes, as well as the control cell, which used carbon felt as the anode. Both Ni-800 and Control anodes started with a lower OCV value of around 150 ± 6.1 mV, while Co-800 and CW-800 anodes started at 231 ± 2.6 mV and 274 ± 3.1 mV, respectively. The Co-800 had a higher rate of increase in voltage, reaching stabilization at the beginning of the second day of operation, followed by the Ni-800 anode on the third day of operation. In contrast, the control cell reached a state of stabilization after 85 h of operation. However, they all stabilized at almost the same voltage value of around 336 ± 13.5 mV. On the other hand, the CW-800 anode demonstrated a very high rate of increase in OCV, increasing dramatically compared to the other anodes used, and reached a stabilized value of 823 mV on the fourth day of operation.

Polarization curves shown in Fig. 6 describe the relationship between the cell voltage and the corresponding current density. It's evident that the CW-800 anode had the highest value of current density of 4322 mA/m^2, followed by the Ni-800 anode with a maximum current density of 2065 mA/m^2, the Co-800 anode with a value of 760 mA/m^2, and the carbon felt anode with a current density value of 508 mA/m^2. Another important insight provided by the polarization curve is the internal resistance of the microbial fuel cell, which is equal to the slope of the polarization curve. It's noteworthy that all polarization curves are mostly linear with a very small deviation at the maximum current density region. This linearity in polarization curves indicates that the dominant type of losses in the assembled MFCs is ohmic losses. However, it's mentioned in literature that linear polarization curves are most often encountered in MFCs [55]. The internal resistance of the MFC can be concluded from the polarization curve by calculating its slope. The lowest internal resistance was observed in the cell assembled with the Ni-800 anode, at a value of 1108 Ω, followed by the CW-800 anode, with a resistance of 1211 Ω, and the Co-800 anode, with a value of 1243 Ω. All cells had relatively lower resistance than the control cell (2200 Ω).

Regarding generated power density, Fig. 7 displays power density curves for all assembled cells, which are calculated by multiplying the cell voltage values by their corresponding current density values on the polarization curve. Obviously, the CW-800 anode demonstrated the highest power density value of 904.6 mW/m^2, significantly outperforming all other anodes used. The maximum power density recorded for the Ni-800 anode is 170.3 mW/m^2, which is almost 20% of the power density generated by the CW-800 anode. Lower than the Ni-800 anode, the Co-800 anode had a maximum power density of 71.2 mW/m^2, followed by the carbon felt anode, which had the lowest power density of 42 mW/m^2. These results are interesting because, despite the modification of the carbonized cabbage core using metal nanoparticles and the reduced electrode resistance of the Ni-800 and Co-800 anodes, they were significantly outperformed by the cell assembled with the CW-800 anode, indicating that the CW-800 anode was more favorable for bacterial adhesion on its surface. This significant performance difference may also be attributed to the change in the microbial consortia that can attach to the anode surface and form a biofilm. It's widely known that some bacterial strains cannot thrive in environments with high concentrations of heavy metals. In microbial fuel cells, the ability of electrogenic bacteria to thrive on the anode surface and oxidize organic pollutants is a key factor in cell performance [42]. Moreover, heavy metals can have a profoundly negative impact on the metabolism and cell functions of various types of microorganisms responsible for generating the electric current in microbial fuel cells [55].

These results highlight the fact that the performance of a microbial fuel cell depends on the combination of several critical factors that must be considered conjointly, which means that modifying the anode structure can have a negative effect on the microbial fuel cell's performance. Moreover, it's recommended to create a balance between the concentration of the heavy metals on the surface of the anode or use electrogenic bacterial strains that can withstand high heavy metal concentrations [56].

Cyclic voltammetry provides two important insights about the proposed electrode. First, the presence of any compounds that can be oxidized within the anode structure can be inferred from the presence of redox peaks in the cyclic voltammogram. Second, estimating the specific capacitance of the anode. Second, estimating the specific capacitance of the anode. Specific capacitance can be described as the area under the

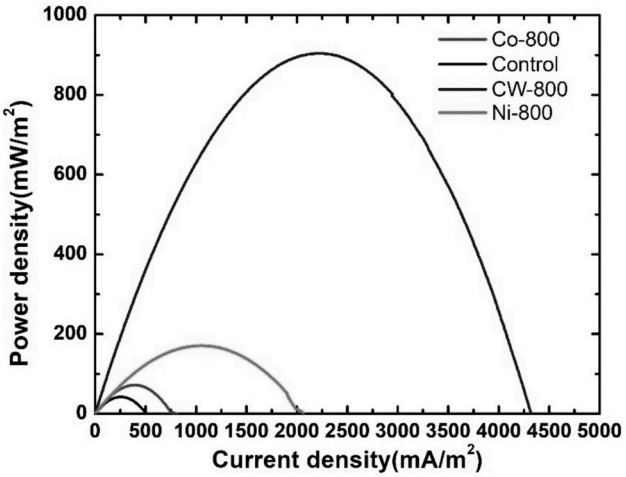

Fig. 8. Power density curves for assembled cells.

Table 4
Comparison with recent MFC studies.

Anode	Cathode	Substrate	Power density	Ref
Carbonized loofah sponge	Air cathode	Acetate	1090 ± 72 mW/m^2	[29]
Carbonized cotton textile	Air cathode	Acetate	931 mW/m^2	[57]
graphene/chitosan/Fe_3O_4 beads	Potassium ferricyanide ($K_3Fe(Cn)_6$)	Acetate	17.823 W/m^3	[58]
porous carbon monolith derived from wax gourd	Phosphate buffer solution + KCl	Sodium acetates	1438.8 mW/m^2	[59]
3D hierarchical porous Co–N–C	Air cathode	Glucose	426.9 ± 7.87 mW/m^2	[60]
Ni thin film on carbon felt	Oxygen in phosphate buffer solution	Glucose	130.72 mW/m^2	[61]
Carbon cloth modified with Ni nanoparticles	Air cathode	Manure wastewater	107.27 mW/m^2	[62]
Activated carbon modified with cobalt nano flakes	Air cathode	Domestic wastewater	576.9 mW/m^2	[63]
spinel cobalt ferrite hierarchical flower-like microspheres	Potassium ferricyanide ($K_3Fe(Cn)_6$)	Glucose	1964 mW/m^2	[64]
Carbonized cocklebur fruit	Air cathode	Acetate	572 ± 24 μW/m^2	[65]
Carbonized cabbage stalk	Potassium ferricyanide ($K_3Fe(Cn)_6$)	Sugarcane wastewater	904.6 ± 11 mW/m^2	

cyclic voltammogram curve. Materials with high specific capacitance have a good ability to absorb ionic and partially ionic compounds. Obviously, neither the Ni-800 nor the Co-800 anodes had any oxidizable or reducible compounds on their surface, as indicated by the absence of redox peaks in the cyclic voltammograms. Moreover, the Ni-800 anode had slightly higher specific capacitance than the Co-800 anode.

Fig. 8 shows the cyclic voltammograms for the modified anodes using a scan rate of 1 mv/s.

Table 4 shows a comparison of previous work related to 3D electrodes in MFCs. It's noteworthy that using simple carbon sources, such as glucose and acetates, is very common in MFCs; however, using real wastewater offers a more realistic and practical insight into the performance of the proposed MFC system, providing the opportunity to discover new electrogenic microorganisms.

Based on power consumption and chemical costs, the cost of producing one cubic meter of catalyzed carbonized cabbage stalk is approximately $ 7.90. Despite being slightly higher than the cost of carbonizing biomass without a catalyst, it's significantly lower than the price of commercially available carbon anodes, such as carbon cloth ($100-$ 1000 per m^2) and carbon brush ($ 270 per m^3). Additionally, lowering the metal concentration has a great potential to decrease the cost of the process.

3.3. COD removal efficiency

Another significant standard to evaluate the performance of microbial fuel cells is COD removal ratio. COD removal efficiency refers to the ability of microorganisms to degrade organic pollutants in wastewater. After a period of 7 days, samples were taken from each cell, and after digestion, the absorbance value was measured using a spectrophotometer, and COD content was determined using the standard curve for both influent and effluent of MFCs. COD removal ratio was calculated using the following equation:

$$\text{COD removal} = \frac{COD_{in} - COD_{out}}{COD_{in}} \times 100$$

The influent COD for all cells was 72,000 mg/l which is a significantly high value compared to domestic sewage and other types of industrial wastewater. The COD value for the effluent of the cells assembled with CW-800, Ni-800 and Co-800 was 29,640, 32531 and 38,430 corresponding to COD removal ratios of 58.8%, 54.8% and 46.6% respectively, Obviously, the Ni-800 cell demonstrated a slightly less COD removal ratio than the CW-800 while the CO-800 cell exhibited the lowest COD removal among all assembled cells. The difference in COD removal ratios can be attributed to the effect metals nanoparticles had on the microbial community on the surface of the anode which is confirmed with the total viable count analysis.

It's noteworthy that despite removing a tremendous amount of organic pollutants, the COD of the effluent is still significantly high which highlights the fact that MFCs can't treat wastewaters with high organic loading and need further treatment techniques.

3.4. Bacterial analysis

3.4.1. Bacterial analysis results

The plate count method was applied to the influent wastewater and effluent of all assembled cells using a media of nutrient agar to determine the total viable count (TVC) and evaluate the effect of adding the metal particles on the ecosystem in the wastewater. It was found that the

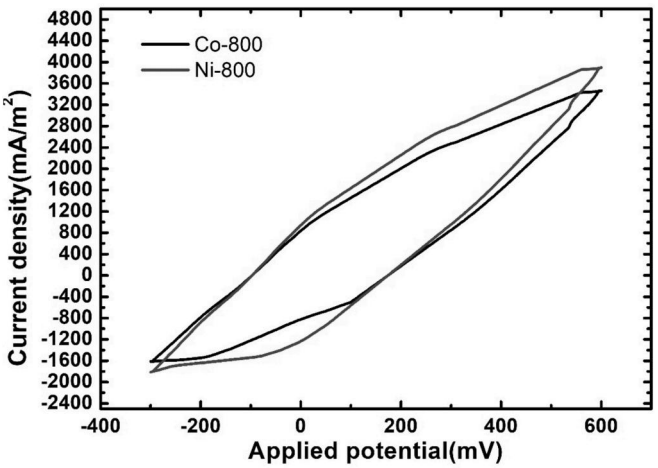

Fig. 9. Cyclic voltammetry for MFC assembled with cabbage core anode.

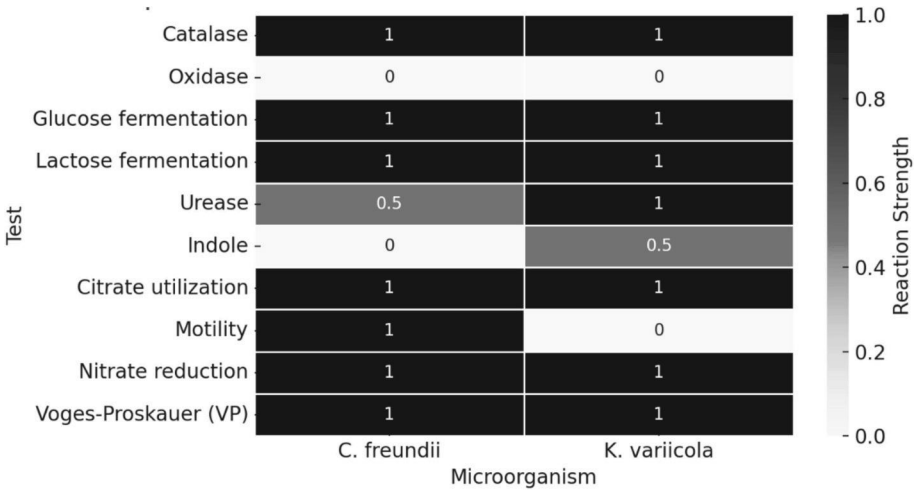

Fig. 10. Heatmap of Predicted Biochemical Reaction Profiles for *Citrobacter freundii* and *K. variicola*. This heatmap illustrates the predicted outcomes of key biochemical tests performed by VITEK on *Citrobacter freundii* and *Klebsiella variicola*. The colour gradient represents the reaction strength, where 1.0 indicates a positive result, 0.0 indicates a negative result, and 0.5 denotes a variable or strain-dependent reaction. Biochemical tests include catalase, oxidase, glucose and lactose fermentation, urease, indole, citrate utilization, motility, nitrate reduction, and Voges-Proskauer (VP) test.

TVC of the influent wastewater is 12.8 × 10ˆ5 cfu/ml. The TVC of the effluent from the CW-800 slightly increased to 13 × 10 ˆ5 cfu/ml. On the other hand, the TVC of the Ni-800 and Co-800 dropped to 5.6 × 10 ˆ5 and 4.3 × 10 ˆ5, respectively. The decrease in the TVC of the Ni-800 and Co-800 indicates that bacterial strains present in the wastewater couldn't withstand the metal concentration on the anodes.

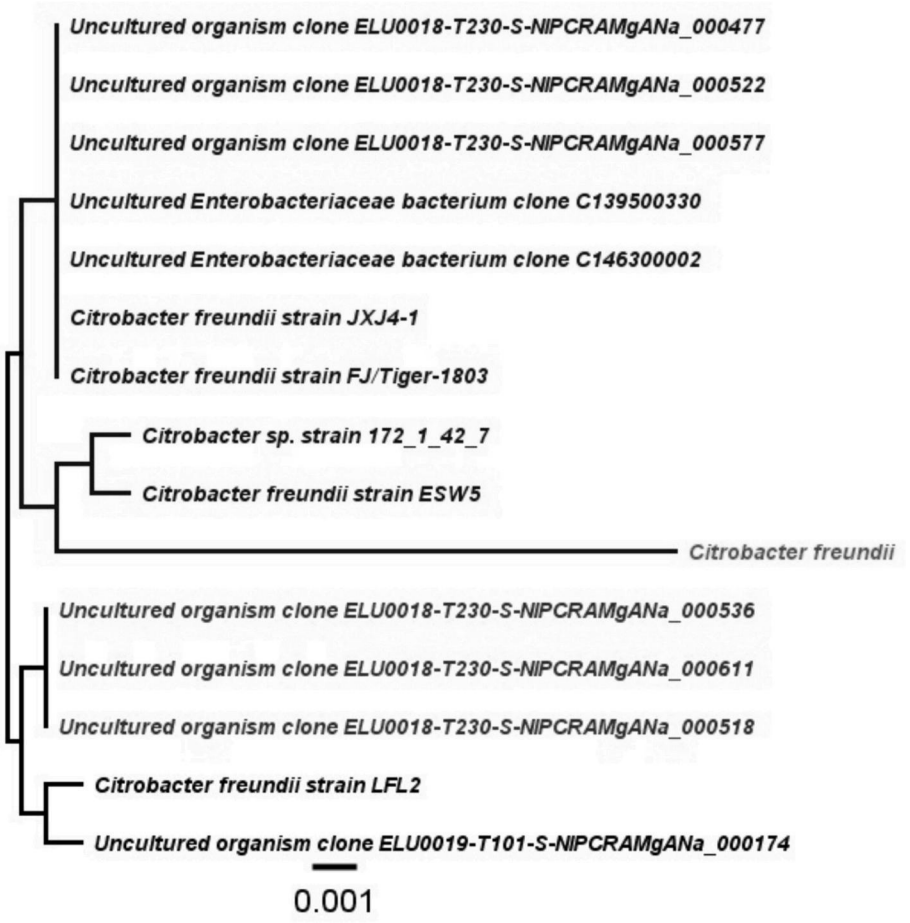

Fig. 11. Phylogenetic tree of *Citrobacter freundii S2* strain based on 16S rRNA gene sequences. A phylogenetic tree was constructed to analyze the evolutionary relationships among different *Citrobacter* strains using 16S rRNA gene sequences. The tree includes multiple strains of *Citrobacter freundii* and uncultured bacterial clones. Different clades are colour-coded to distinguish major groupings. Branch support values (posterior probabilities) are indicated at the nodes, with values closer to 1 signifying stronger support. The scale bar represents genetic distance (0.001), illustrating sequence divergence. Our strain S2 is highlighted in red. (For interpretation of the references to colour in this figure legend, the reader is referred to the web version of this article.)

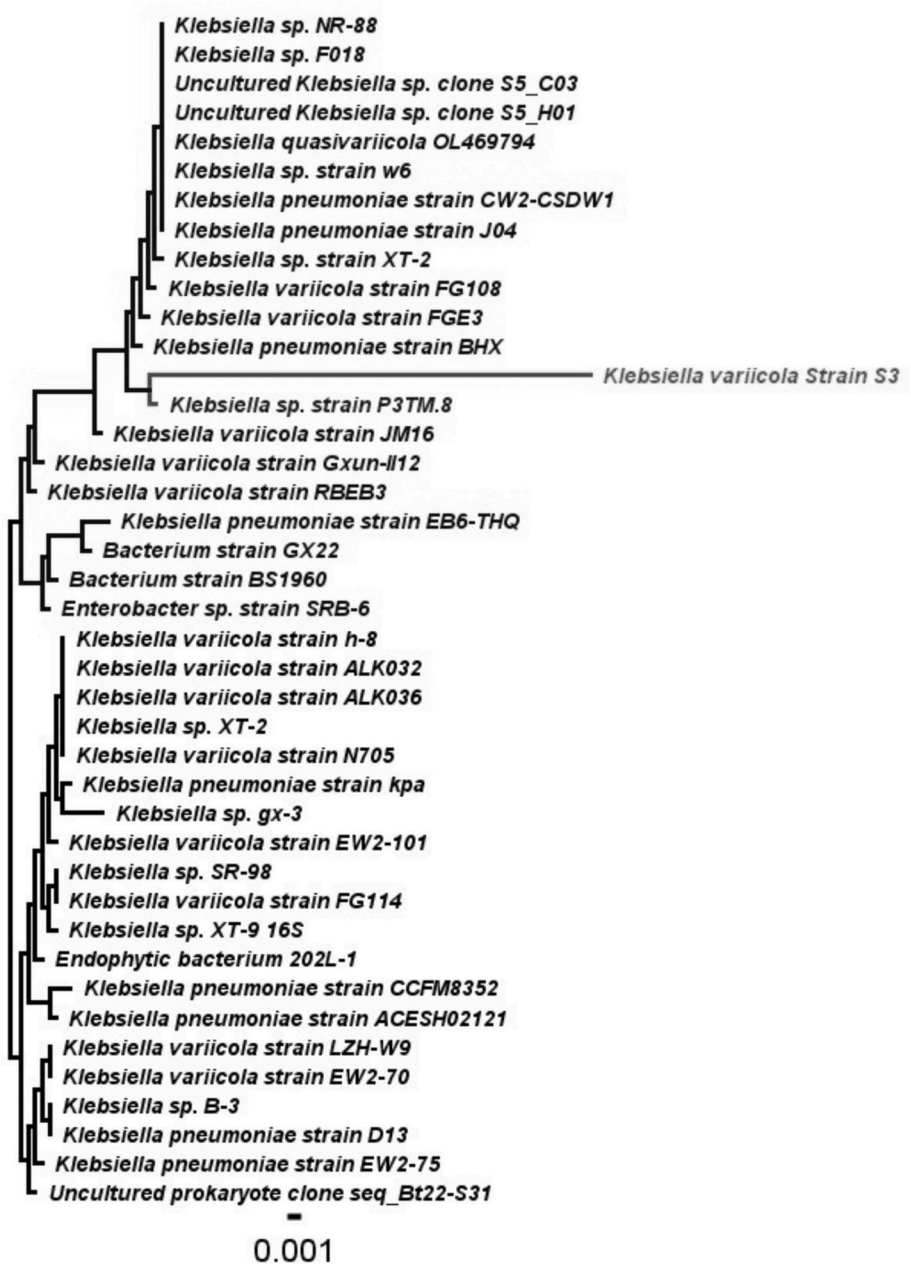

Fig. 12. Phylogenetic tree of *Klebsiella* strains based on 16S rRNA gene sequences. A phylogenetic tree was constructed to analyze the evolutionary relationships among different *Klebsiella* strains using 16S rRNA gene sequences. The tree includes multiple strains of *Klebsiella variicola*, *Klebsiella pneumoniae*, and *Klebsiella quasivariicola*. Different clades are colour-coded to distinguish major groupings. Branch support values (posterior probabilities) are indicated at the nodes, with values closer to 1 signifying stronger support. The scale bar represents genetic distance (0.001), illustrating sequence divergence. Our strain *K. variicola* strain S3 is highlighted in red colour. (For interpretation of the references to colour in this figure legend, the reader is referred to the web version of this article.)

The 16S rRNA gene partial sequences obtained in this study were deposited in the NCBI GenBank database. The accession numbers are as follows: _*Citrobacter freundii*_ strain S2 (GenBank: PV809873.1) and _*Klebsiella variicola*_ strain S3 (GenBank: PX136842.1).

Microorganism identification was performed using the bioMérieux VITEK MS system. The analysis of samples (S2 and S3) yielded a confident identification of *Citrobacter freundii S2* and *Klebsiella variicola S3* (refer to Supplementary file S). Comparative biochemical profiling of *Citrobacter freundii* and *Klebsiella variicola* was conducted using VITEK predictions, and the outcomes are presented as a heatmap Fig. 9. The results demonstrated that both isolates exhibited positive reactions (reaction strength = 1.0) for catalase, glucose fermentation, citrate utilization, nitrate reduction, and the Voges-Proskauer (VP) test. Both strains tested negative (reaction strength = 0.0) for oxidase, motility, and indole production, with *C. freundii* also showing a negative result for lactose fermentation, while *K. variicola* was positive. Urease activity was displayed by *C. freundii*, showing a variable reaction (0.5), and *K. variicola* exhibited a positive result (1.0). These findings reflect the close but distinct biochemical profiles of the two species.

The constructed phylogenetic tree effectively illustrates the evolutionary relationships among *Citrobacter freundii* strains, related *Citrobacter* species, and a set of uncultured *Enterobacteriaceae* clones. Notably, several uncultured organism clones clustered closely with *C. freundii* reference strains (JXJ4-1, FJ/Tiger-1803, ESW5), indicating a strong genetic affiliation and suggesting their probable identity as *C. freundii*-related taxa. Interestingly, a distinct subclade comprising other uncultured clones (colored in purple) formed a separate lineage, with relatively closer proximity to *C. freundii* strain LFL2 and another

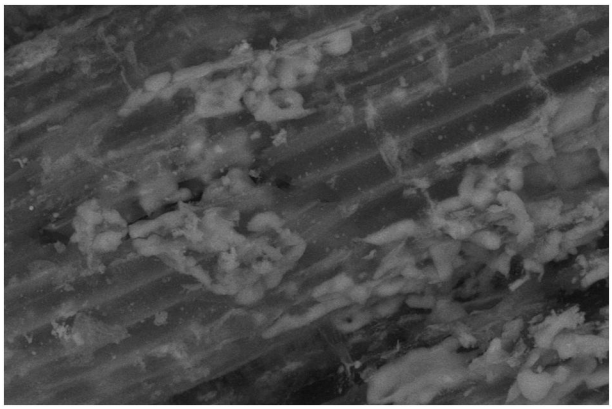

Fig. 13. SEM image showing bacterial species attached to the surface of the Ni-800 anode.

uncultured clone ELU0019-T101, potentially representing a divergent or uncharacterized *Citrobacter* lineage. The tree topology reinforces the presence of considerable genetic heterogeneity within the *Citrobacter freundii* complex, highlighting the potential of environmental isolates and uncultured clones to expand our understanding of *Citrobacter* phylogenetics. The robust clustering pattern and low evolutionary distance (scale bar = 0.001) also suggest high sequence similarity among these strains, particularly within the dominant *C. freundii* clade, as shown in Fig. 10.

The phylogenetic tree based on 16S rRNA gene sequences reveals the taxonomic positioning of our isolate, *Klebsiella variicola* strain S3 (highlighted in red). Strain S3 clustered closely with other *Klebsiella variicola* strains, such as FG108, FGE3, and JM16, forming a distinct subclade within the *Klebsiella variicola* lineage. This phylogenetic arrangement supports the identification of S3 as a member of the *Klebsiella variicola* species. The close relatedness to both *K. pneumoniae* and other *K. variicola* strains suggests potential genomic and functional similarities, which merit further comparative genomic and phenotypic characterization. The robustness of the tree topology and branch distances (scale bar: 0.001 substitutions per nucleotide position) provides a reliable framework for strain classification and evolutionary inference (Fig. 11). Interestingly, *Klebsiella variicola* strain S3 forms a separate branch closely related to *K. pneumoniae* strain BHX and other nearby *Klebsiella variicola* strains. However, it doesn't cluster within the tighter clades of other *K. variicola* strains, which are shown lower in the tree due to genetic differences (Fig. 12).

3.4.2. Bacterial analysis discussion

In this study, biochemical tests performed by the VITEK® system provided valuable identification for *Citrobacter freundii* and *Klebsiella variicola*. Both isolates displayed comparable predicted patterns for several reactions. The heatmap visualization of predicted reaction profiles effectively highlights these similarities and differences. Despite the reliability of VITEK®, it should be noted that phenotypic variability, environmental adaptation, and strain-level differences can influence test outcomes. The phylogenetic analysis presented in this study provides valuable insights into the genetic diversity and evolutionary relationships among *Citrobacter freundii* S2 strain, related *Citrobacter* species, and environmental *Enterobacteriaceae* clones. The clustering of several uncultured organism clones alongside established *C. freundii* strains (JXJ4-1, FJ/Tiger-1803, and ESW5) suggests that these environmental isolates likely represent uncharacterized or closely related members of the *C. freundii* lineage. This finding aligns with previous reports indicating the ecological ubiquity and genetic plasticity of *C. freundii*, a species known for its environmental adaptability and opportunistic pathogenicity [66,67]. Fig. 13 demonstrates the accumulation of bacterial species on the surface of the anode, while Fig. 14 shows the TEM images of the isolated strains from the surface of the anode.

Moreover, the formation of a distinct subclade comprising uncultured clones (ELU0018-T230 series) alongside *C. freundii* strain LFL2 and another uncultured isolate (ELU0019-T101) highlights the presence of divergent *Citrobacter*-like taxa within environmental samples. These sequences, while related to the *C. freundii* cluster, exhibit sufficient phylogenetic separation to suggest potential novel lineages or subspecies. Similar observations have been reported in environmental microbiome surveys, where metagenomic and molecular approaches revealed significant cryptic diversity within *Enterobacteriaceae* lineages [66,67]. Such findings underscore the importance of environmental microbial surveys and molecular phylogenetics in uncovering hidden microbial diversity, particularly within taxa traditionally considered clinically relevant. The overall low genetic distance within the main *C. freundii* clade (indicated by the scale bar of 0.001) confirms a high degree of sequence conservation among these strains, reinforcing their close taxonomic relationship. However, the emergence of phylogenetically distinct clusters may have implications for antimicrobial resistance, environmental persistence, and pathogenic potential, warranting further genomic and phenotypic characterization [68,69]. Collectively, these results contribute to a growing body of evidence emphasizing the genetic complexity within *Citrobacter* species and highlight the value of phylogenetic reconstruction in delineating taxonomic boundaries and identifying novel bacterial taxa from environmental sources [70,71]. The current study reports the Isolation and phylogenetic characterization of a novel strain identified as *Klebsiella variicola* strain S3.

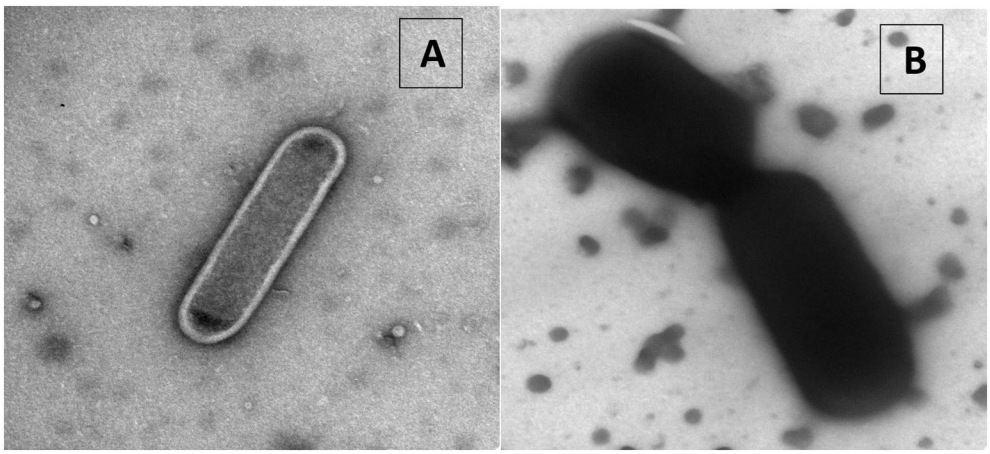

Fig. 14. TEM images showing the isolated bacterial species A: *Citrobacter freundii,* B*: Klebsiella variicola.*

Phylogenetic analysis based on 16S rRNA gene sequences revealed that strain S3 clustered closely with *Klebsiella pneumoniae* strain BHX and several *Klebsiella variicola* strains but notably formed a separate branch within the phylogenetic tree. This branching pattern suggests a degree of genetic divergence from other members of the *K. variicola* clade, indicating possible ecological, genetic, or evolutionary distinctiveness. The genus *Klebsiella* is taxonomically complex, with closely related species such as *K. pneumoniae, K. variicola*, and *K. quasipneumoniae* often displaying high 16S rRNA sequence similarity, making precise identification challenging using 16S rRNA alone [67]. However, even within highly conserved genes like 16S rRNA, minor sequence variations can reveal sub-lineages or ecotypes, as observed in our strain S3. Its separate branching could be attributed to unique nucleotide substitutions in phylogenetically informative regions of the 16S rRNA gene, which have been reported to influence clade separation in other *Klebsiella* strains [70]. Previous studies have highlighted the environmental versatility of *K. variicola*, which, unlike its clinically dominant relative *K. pneumoniae*, is often isolated from plant, soil, and water environments, yet has increasingly been implicated in opportunistic human infections [72,73]. The distinct phylogenetic positioning of strain S3 may, therefore, reflect ecological adaptation, a phenomenon described in environmental *Klebsiella* isolates from various niches [74]. It is possible that strain S3 has acquired unique mutations or undergone horizontal gene transfer events contributing to its divergence. Although 16S rRNA gene analysis provides valuable preliminary taxonomic insights, its limited resolution for differentiating closely related *Klebsiella* species and strains is well-documented [75]. Thus, the current phylogenetic placement of strain S3 warrants further confirmation through multilocus sequence analysis (MLSA) or whole-genome sequencing (WGS), which offer greater discriminatory power, or by calculating average nucleotide identity (ANI) values [76]. Moreover, the proximity of strain S3 to *K. pneumoniae* strain BHX in the phylogenetic tree suggests potential genomic similarities that might have implications for antimicrobial resistance profiles or virulence factors. Recent genomic analyses have reported overlapping resistance gene repertoires and pathogenicity islands between environmental and clinical *K. variicola* and *K. pneumoniae* strains, underscoring the importance of characterizing environmental isolates, such as strain S3. In conclusion, the phylogenetic analysis positions *Klebsiella variicola* strain S3 as a distinct sub-lineage within the *K. variicola* group, while *Citrobacter freundii* strain S2 clusters within its respective clade, reflecting notable genetic diversity within both species. This highlights the importance of comprehensive genomic characterization to understand better their evolutionary relationships, ecological niches, and functional capacities. Importantly, both strains have demonstrated effective performance in microbial fuel cells (MFCs), and their distinct phylogenetic positions may underpin unique metabolic and electroactive properties. These findings not only emphasize their potential in sustainable energy generation and wastewater treatment but also suggest that further investigation into their genomic and metabolic frameworks could enhance their application in bioelectrochemical systems.

4. Conclusions

This study investigated the effect of catalyzing the carbonization of biomass using Nickel and Cobalt and using the resulting carbonaceous materials as anodes in MFCs. The addition of nickel and cobalt to the carbonization process catalyzes the formation of more graphitic domains within the electrode structure, which significantly increases the material's conductivity, enhances the BET surface area and pore size, and slightly improves the extracellular electron transfer process. However, the metal-doped electrodes were significantly outperformed by the CW-800 anode in terms of OCV and power density by around 5.32-fold for the NI-800 anode and 12.7-fold for the Co-800 anode. This can be attributed to the decrease in biocompatibility and the toxic effect that metals have on electroactive microorganisms. These results emphasize the importance of balancing the concentration of metals incorporated with the carbonaceous materials used in MFCs. Additionally, they emphasize the importance of investigating more extremophilic electroactive microorganisms that can tolerate the high metal concentrations present on the electrode surface.

CRediT authorship contribution statement

Ahmed Abotaleb: Writing – review & editing, Writing – original draft, Validation, Methodology, Investigation, Formal analysis, Data curation. **Ashraf Ahmed:** Writing – review & editing, Validation, Methodology, Investigation. **Dina H. Amin:** Writing – review & editing, Writing – original draft, Visualization, Methodology, Investigation, Formal analysis, Data curation. **Toka Khairy:** Writing – original draft, Visualization, Methodology, Investigation. **Khaled A. Abd El-Rahem:** Writing – original draft, Validation, Methodology, Formal analysis. **Abeer El Shahawy:** Writing – review & editing, Writing – original draft, Validation, Supervision, Methodology, Data curation, Conceptualization.

Funding

This research was funded by the Science, Technology &Innovation Funding Authority (STDF) Grant, which supported this work from the STDF Fund within the framework of the "Egyptian American Cooperation Grant" call 20, Egypt (Project ID 45898, C1130, 2021).

Declaration of competing interest

The authors declare that they have no known competing financial interests or personal relationships that could have appeared to influence the work reported in this paper.

Appendix A. Supplementary data

Supplementary data to this article can be found online at https://doi.org/10.1016/j.jwpe.2026.109482.

Data availability•

The datasets used and/or analyzed during the current study are available from the corresponding author upon reasonable request.•

All data generated or analyzed during this study are included in this published article.

References

[1] B.E. Logan, J.M. Regan, Microbial fuel cells—challenges and applications, Environ. Sci. Technol. 40 (17) (2006) 5172–5180.
[2] B.E. Logan, B. Hamelers, R. Rozendal, U. Schröder, J. Keller, S. Freguia, P. Aelterman, W. Verstraete, Microbial fuel cells: methodology and technology, Environmental Science & Technology 40 (17) (2006) 5181–5192, https://doi.org/10.1021/es0605016.
[3] B.E. Logan, Microbial Fuel Cells, John Wiley & Sons, 2008.
[4] A.E. Franks, K.P. Nevin, Microbial fuel cells, a current review, Energies 3 (5) (2010) 899–919.
[5] A.J. Slate, K.A. Whitehead, D.A. Brownson, C.E. Banks, Microbial fuel cells: an overview of current technology, Renew. Sust. Energ. Rev. 101 (2019) 60–81.
[6] C. Santoro, C. Arbizzani, B. Erable, I. Ieropoulos, Microbial fuel cells: from fundamentals to applications. A review, J. Power Sources 356 (2017) 225–244.
[7] J.V. Boas, V.B. Oliveira, M. Simões, A.M. Pinto, Review on microbial fuel cells applications, developments and costs, J. Environ. Manag. 307 (2022) 114525.
[8] S. Gupta, A. Patro, Y. Mittal, S. Dwivedi, P. Saket, R. Panja, T. Saeed, F. Martínez, A.K. Yadav, The race between classical microbial fuel cells, sediment-microbial fuel cells, plant-microbial fuel cells, and constructed wetlands-microbial fuel cells: applications and technology readiness level, Sci. Total Environ. 879 (2023) 162757.
[9] N.A. Barakat, K.A. Khalil, Sustainable electrocatalytic cathodes and biomass-derived anodes for high-performance microbial fuel cells, in: Proceedings of the International Conference on Sustainability: Developments and Innovations, 2024.
[10] D.R. Lovley, Microbial fuel cells: novel microbial physiologies and engineering approaches, Curr. Opin. Biotechnol. 17 (3) (2006) 327–332.

[11] A. Dewan, H. Beyenal, Z. Lewandowski, Scaling up microbial fuel cells, Environ. Sci. Technol. 42 (20) (2008) 7643–7648.

[12] Y. Qiao, C.M. Li, S.J. Bao, Q.L. Bao, Carbon nanotube/polyaniline composite as anode material for microbial fuel cells, J. Power Sources 170 (1) (2007) 79–84.

[13] A.A. Yaqoob, M.N.M. Ibrahim, A.S. Yaakop, K. Umar, A. Ahmad, Modified graphene oxide anode: a bioinspired waste material for bioremediation of Pb2+ with energy generation through microbial fuel cells, Chem. Eng. J. 417 (2021) 128052.

[14] H. Xu, H. Xu, Y. Chen, Q. Wen, C. Lin, H. Gao, Z. Qiu, L. Yang, X. Pan, The role of binary transition metal Cobalt-Nickel sulfide as an anode catalyst in specifically selection of Desulfuromonas and improved performance of microbial fuel cell, Chemical Engineering Journal 470 (2023) 144163, https://doi.org/10.1016/j.cej.2023.144163.

[15] T. Mei, C. Cong, Q. Huang, T.S. Song, J. Xie, Effect of 3D carbon electrodes with different pores on solid-phase microbial fuel cell, Energy Fuel 34 (12) (2020) 16765–16771.

[16] R. Wang, D. Liu, M. Yan, L. Zhang, W. Chang, Z. Sun, Three-dimensional high performance free-standing anode by one-step carbonization of pinecone in microbial fuel cells, Bioresource Technology 292 (2019) 121956, https://doi.org/10.1016/j.biortech.2019.121956.

[17] A.A. Yaqoob, M.N.M. Ibrahim, C. Guerrero-Barajas, Modern trend of anodes in microbial fuel cells (MFCs): an overview, Environ. Technol. Innovation 23 (2021) 101579.

[18] K. Scott, G.A. Rimbu, K.P. Katuri, K.K. Prasad, I.M. Head, Application of modified carbon anodes in microbial fuel cells, Process. Saf. Environ. Prot. 85 (5) (2007) 481–488.

[19] FAOSTAT, Statistics for Climate Change in Agriculture, Forestry and Other Land, 2019.

[20] D. Khukutapan, N. Chiewchan, S. Devahastin, Characterization of nanofibrillated cellulose produced by different methods from cabbage outer leaves, J. Food Sci. 83 (6) (2018) 1660–1667.

[21] D.W. Rutherford, R.L. Wershaw, C.E. Rostad, C.N. Kelly, Effect of formation conditions on biochars: compositional and structural properties of cellulose, lignin, and pine biochars, Biomass Bioenergy 46 (2012) 693–701.

[22] P. Yang, Y. Han, L. Xue, Y. Gao, J. Liu, W. He, Y. Feng, Effect of lignocellulosic biomass components on the extracellular electron transfer of biochar-based microbe-electrode in microbial electrochemical systems, J. Water Process Eng. 59 (2024) 105013.

[23] A.Y. Radeef, Z.Z. Ismail, Improvement of bioenergy generation using innovative application of food waste materials for coating carbon nanotubes-loaded bioanode in 3D-microbial fuel cells, Int. J. Hydrog. Energy 48 (49) (2023) 18835–18844.

[24] N.A. Barakat, M.M.A. Hameed, O.A. Fadali, O.H. Abdelraheem, R.A. Hefny, H. M. Moustafa, Graphitized corncob 3D Biomass–driven anode for high performance batch and continuous modes air–cathode microbial fuel cells working by domestic wastewater, Int. J. Hydrog. Energy 48 (98) (2023) 38854–38869.

[25] J. Liu, C. Chu, L. Wei, J. Feng, J. Shen, Iron/cobalt-decorated nitrogen-rich 3D layer-stacked porous biochar as high-performance oxygen reduction air-cathode catalyst in microbial fuel cell, Biosens. Bioelectron. 222 (2023) 114926.

[26] L. Meng, M. Feng, J. Sun, R. Wang, F. Qu, C. Yang, W. Guo, High-performance free-standing microbial fuel cell anode derived from Chinese date for enhanced electron transfer rates, Bioresour. Technol. 353 (2022) 127151.

[27] J.Z. Sun, Q.C. Shu, H.W. Sun, Y.C. Liu, X.Y. Yang, Y.X. Zhang, G. Wang, High-performance macroporous free-standing microbial fuel cell anode derived from grape for efficient power generation and brewery wastewater treatment, Molecules 29 (12) (2024) 2936.

[28] M. Rethinasabapathy, J.H. Lee, K.C. Roh, S.M. Kang, S.Y. Oh, B. Park, G. Lee, Y. L. Cha, Y.S. Huh, Silver grass-derived activated carbon with coexisting micro-, meso-and macropores as excellent bioanodes for microbial colonization and power generation in sustainable microbial fuel cells, Bioresource Technology 300 (2020) 122646, https://doi.org/10.1016/j.biortech.2019.122646.

[29] Y. Yuan, S. Zhou, Y. Liu, J. Tang, Nanostructured macroporous bioanode based on polyaniline-modified natural loofah sponge for high-performance microbial fuel cells, Environ. Sci. Technol. 47 (24) (2013) 14525–14532.

[30] M. Li, Y.W. Li, Q.Y. Cai, S.Q. Zhou, C.H. Mo, Spraying carbon powder derived from mango wood biomass as high-performance anode in bio-electrochemical system, Bioresour. Technol. 300 (2020) 122623.

[31] C. Wang, X. Chai, F. Yu, J. Ma, Novel three-dimensional electrode structures with urchin-like pore canal for high-performance microbial fuel cells, Electrochim. Acta 475 (2024) 143601.

[32] Y. Chen, F. Zhao, Y. Pu, X. Lin, H. Yin, X. Tang, Nano-Fe3O4 coated on carbon monolith for anode enhancement in microbial fuel cells, J. Environ. Chem. Eng. 11 (2) (2023) 109608.

[33] S. Singh, N. Verma, Fabrication of Ni nanoparticles-dispersed carbon micro-nanofibers as the electrodes of a microbial fuel cell for bio-energy production, Int. J. Hydrog. Energy 40 (2) (2015) 1145–1153.

[34] Y. Qiao, X.S. Wu, C.X. Ma, H. He, C.M. Li, A hierarchical porous graphene/nickel anode that simultaneously boosts the bio-and electro-catalysis for high-performance microbial fuel cells, RSC Adv. 4 (42) (2014) 21788–21793.

[35] F. Mahmoodzadeh, N. Navidjouy, S. Alizadeh, M. Rahimnejad, Investigation of microbial fuel cell performance based on the nickel thin film modified electrodes, Sci. Rep. 13 (1) (2023) 20755.

[36] N. Jiang, J. Song, M. Yan, Y. Hu, M. Wang, Y. Liu, M. Huang, Iron cobalt-doped carbon nanofibers anode to simultaneously boost bioelectrocatalysis and direct electron transfer in microbial fuel cells: characterization, performance, and mechanism, Bioresour. Technol. 367 (2023) 128230.

[37] E.W. Rice, R.B. Baird, A.D. Eaton, L.S. Clesceri, Standard Methods for the Examination of Water and Wastewater, 2012.

[38] S.D. Behera, U. Kumari, R. Shankar, P. Mondal, Performance analysis of a double-chambered microbial fuel cell employing a low-cost sulfonated polystyrene proton exchange membrane, Ionics 24 (11) (2018) 3573–3590.

[39] L. Lagacé, M. Pitre, M. Jacques, D. Roy, Identification of the bacterial community of maple sap by using amplified ribosomal DNA (rDNA) restriction analysis and rDNA sequencing, Appl. Environ. Microbiol. 70 (4) (2004) 2052–2060.

[40] J. Sambrook, E.F. Fritsch, T. Maniatis, Molecular Cloning: A Laboratory Manual (No. Ed. 2, pp. xxxviii+-1546), 1989.

[41] M.N. Price, P.S. Dehal, A.P. Arkin, FastTree: computing large minimum evolution trees with profiles instead of a distance matrix, Mol. Biol. Evol. 26 (7) (2009) 1641–1650.

[42] B.E. Logan, Exoelectrogenic bacteria that power microbial fuel cells, Nat. Rev. Microbiol. 7 (5) (2009) 375–381.

[43] P. Chong, B. Erable, A. Bergel, Effect of pore size on the current produced by 3-dimensional porous microbial anodes: a critical review, Bioresour. Technol. 289 (2019) 121641, https://doi.org/10.1016/j.biortech.2019.121641.

[44] B.S. Girgis, Y.M. Temerk, M.M. Gadelrab, I.D. Abdullah, X-ray diffraction patterns of activated carbons prepared under various conditions, Carbon Sci. 8 (2) (2007) 95–100.

[45] K. Hadjiivanov, Identification and characterization of surface hydroxyl groups by infrared spectroscopy, in: Advances in Catalysis vol. 57, Academic Press, 2014, pp. 99–318.

[46] A.G. Kumar, A. Singh, H. Komber, B. Voit, B.R. Tiwari, M.T. Noori, M. M. Ghangrekar, S. Banerjee, Novel sulfonated Co-poly (ether imide) s containing trifluoromethyl, fluorenyl and hydroxyl groups for enhanced proton exchange membrane properties: Application in microbial fuel cell, ACS Applied Materials & Interfaces 10 (17) (2018) 14803–14817, https://doi.org/10.1021/acsami.8b03452.

[47] U. Schröder, Anodic electron transfer mechanisms in microbial fuel cells and their energy efficiency, Phys. Chem. Chem. Phys. 9 (21) (2007) 2619–2629.

[48] V. Ţucureanu, A. Matei, A.M. Avram, FTIR spectroscopy for carbon family study, Crit. Rev. Anal. Chem. 46 (6) (2016) 502–520.

[49] I. Zojaji, A. Esfandiarian, J. Taheri-Shakib, Toward molecular characterization of asphaltene from different origins under different conditions by means of FT-IR spectroscopy, Adv. Colloid Interf. Sci. 289 (2021) 102314.

[50] O. Francioso, S. Sanchez-Cortes, S. Bonora, M.L. Roldán, G. Certini, Structural characterization of charcoal size-fractions from a burnt Pinus pinea forest by FT-IR, Raman and surface-enhanced Raman spectroscopies, J. Mol. Struct. 994 (1–3) (2011) 155–162.

[51] I.E. Wachs, M.A. Bañares (Eds.), Springer Handbook of Advanced Catalyst Characterization, Springer Nature, 2023.

[52] R. Fu, T.F. Baumann, S. Cronin, G. Dresselhaus, M.S. Dresselhaus, J.H. Satcher, Formation of graphitic structures in cobalt-and nickel-doped carbon aerogels, Langmuir 21 (7) (2005) 2647–2651.

[53] J.B. Parra, J.D. Sousa, R.C. Bansal, J.J. Pis, J.A. Pajares, Characterization of activated carbons by the BET equation—an alternative approach, Adsorpt. Sci. Technol. 12 (1) (1995) 51–66.

[54] Z.-Y. Wu, S.-L. Xu, Q.-Q. Yan, Z.-Q. Chen, Y.-W. Ding, C. Li, H.-W. Liang, S.-H. Yu, Transition metal–assisted carbonization of small organic molecules toward functional carbon materials, Sci. Adv. 4 (7) (2018) eaat0788.

[55] E. Bååth, Effects of heavy metals in soil on microbial processes and populations (a review), Water Air Soil Pollut. 47 (3) (1989) 335–379.

[56] A. Abotaleb, A.M. Saleh, S.E. Ali, N.A. Barakat, S. EL-Shatoury, A. Shaltout, A. El Shahawy, Boosting the performance of microbial fuel cells fed with partially treated buffalo milkmaid wastewater using modified CC/Co anodes: bacterial activity insights, Sustain. Energy Fuels 8 (17) (2024) 3994–4005.

[57] L. Zeng, S. Zhao, M. He, Macroscale porous carbonized polydopamine-modified cotton textile for application as electrode in microbial fuel cells, J. Power Sources 376 (2018) 33–40.

[58] C. Wang, X. Chai, F. Yu, J. Ma, Novel three-dimensional electrode structures with urchin-like pore canal for high-performance microbial fuel cells, Electrochim. Acta 475 (2024) 143601.

[59] Y. Chen, F. Zhao, Y. Pu, X. Lin, H. Yin, X. Tang, Nano-Fe3O4 coated on carbon monolith for anode enhancement in microbial fuel cells, J. Environ. Chem. Eng. 11 (2) (2023) 109608.

[60] Q.R. Pan, P.Y. Jiang, B.L. Lai, Y.B. Qian, L.J. Huang, X.X. Liu, N. Li, Z.Q. Liu, Co, N co-doped hierarchical porous carbon as efficient cathode electrocatalyst and its impact on microbial community of anode biofilm in microbial fuel cell, Chemosphere 291 (2022) 132701, https://doi.org/10.1016/j.chemosphere.2021.132701.

[61] F. Mahmoodzadeh, N. Navidjouy, S. Alizadeh, M. Rahimnejad, Investigation of microbial fuel cell performance based on the nickel thin film modified electrodes, Sci. Rep. 13 (1) (2023) 20755.

[62] A. Abotaleb, A.M. Saleh, S.E. Ali, N.A. Barakat, S. EL-Shatoury, A. Shaltout, A. El Shahawy, Boosting the performance of microbial fuel cells fed with partially treated buffalo milkmaid wastewater using modified CC/Co anodes: bacterial activity insights, Sustain. Energy Fuels 8 (17) (2024) 3994–4005.

[63] H.O. Mohamed, M.A. Abdelkareem, M. Obaid, S.H. Chae, M. Park, H.Y. Kim, N. A. Barakat, Cobalt oxides-sheathed cobalt nano flakes to improve surface properties of carbonaceous electrodes utilized in microbial fuel cells, Chem. Eng. J. 326 (2017) 497–506.

[64] M. Rethinasabapathy, A.E. Vilian, S.K. Hwang, S.M. Kang, Y. Cho, Y.K. Han, J. K. Rhee, Y.S. Huh, Cobalt ferrite microspheres as a biocompatible anode for higher

power generation in microbial fuel cells, Journal of Power Sources 483 (2021) 229170, https://doi.org/10.1016/j.jpowsour.2020.229170.
[65] C. Yang, M. Chen, Y. Qian, L. Zhang, M. Lu, X. Xie, L. Huang, W. Huang, Packed anode derived from cocklebur fruit for improving long-term performance of microbial fuel cells, Science China Materials 62 (5) (2019) 645–652, https://doi.org/10.1007/s40843-018-9368-y.
[66] L. Liu, Y. Feng, Z. Zong, Enterobacteriaceae: Overview of taxonomy, clinical significance, and laboratory identification, in: Y.-W. Tang, C.W. Stratton (Eds.), Advanced Techniques in Diagnostic Microbiology, Springer, 2018, pp. 471–493, https://doi.org/10.1007/978-3-319-99381-4_21.
[67] J.M. Janda, S.L. Abbott, The genus Citrobacter, Clin. Microbiol. Rev. 19 (2) (2006) 312–339, https://doi.org/10.1128/CMR.19.2.312-339.2006.
[68] K.D. Chavda, L. Chen, D.E. Fouts, B.N. Kreiswirth, Comparison of molecular methods for typing multidrug-resistant Klebsiella pneumoniae isolates, J. Clin. Microbiol. 54 (12) (2016) 2897–2902, https://doi.org/10.1128/JCM.01630-16.
[69] M. Yamamoto, M. Nagata, H. Maeda, Phylogenetic diversity and antimicrobial susceptibility of Enterobacteriaceae from environmental and clinical sources, Front. Microbiol. 13 (2022) 890722, https://doi.org/10.3389/fmicb.2022.890722.
[70] C. Rodrigues, V. Passet, A. Rakotondrasoa, T.A. Diallo, A. Criscuolo, S. Brisse, Description of Klebsiella africanensis sp. nov., Klebsiella variicola subsp. tropicalensis subsp. nov., and Klebsiella variicola subsp. variicola* subsp. nov, Res. Microbiol. 170 (3) (2019) 165–170, https://doi.org/10.1016/j.resmic.2019.02.003.
[71] H. Barrios-Camacho, A. Aguilar-Vera, M. Beltrán-Rojel, R. Morales-Espinosa, E. González-Villalobos, I. Martínez-Flores, R. Hernández-Castro, The highly diverse Klebsiella pneumoniae complex includes important human pathogens and environmental species, Microorganisms 7 (9) (2019) 608, https://doi.org/10.3390/microorganisms7090608.
[72] M. Rosenblueth, L. Martínez, J. Silva, E. Martínez-Romero, Klebsiella variicola, a novel species with clinical and plant-associated isolates, Syst. Appl. Microbiol. 27 (1) (2004) 27–35, https://doi.org/10.1078/072320204322881694.
[73] R.M. Martin, M.A. Bachman, Colonization, infection, and the accessory genome of Klebsiella pneumoniae, Front. Cell. Infect. Microbiol. 8 (2018) 4, https://doi.org/10.3389/fcimb.2018.00004.
[74] A. Peix, M.H. Ramírez-Bahena, E. Velázquez, The current status on the taxonomy of Pseudomonas revisited: an update, Infect. Genet. Evol. 29 (2015) 145–161, https://doi.org/10.1016/j.meegid.2014.10.012.
[75] S. Brisse, V. Passet, P.A.D. Grimont, Description of Klebsiella quasipneumoniae sp. nov., a novel species isolated from human infections, and of two subspecies: Klebsiella quasipneumoniae subsp. quasipneumoniae and Klebsiella quasipneumoniae subsp. similipneumoniae, Int. J. Syst. Evol. Microbiol. 64 (Pt 9) (2014) 3146–3151, https://doi.org/10.1099/ijs.0.062737-0.
[76] S.W. Long, S.E. Linson, M. Ojeda Saavedra, C. Cantu, J.J. Davis, T. Brettin, R. J. Olsen, Whole-genome sequencing of human clinical Klebsiella pneumoniae isolates reveals misidentification and misunderstandings of K. Variicola, BMC Genomics 18 (1) (2017) 625, https://doi.org/10.1186/s12864-017-4002-7.